

submitted

From Radio to X-ray: Flares on the dMe Flare Star EV Lacertae

Rachel A. Osten^{1a}

*National Radio Astronomy Observatory
520 Edgemont Road
Charlottesville, VA 22903
Electronic Mail: rosten@nrao.edu*

Suzanne L. Hawley^a

*Astronomy Department
Box 351580
University of Washington
Seattle, WA 98195
Electronic Mail: slh@astro.washington.edu*

Joel C. Allred

*Physics Department
Box 351560
University of Washington
Seattle, WA 98195
Electronic Mail: jallred@u.washington.edu*

Christopher M. Johns-Krull^a

*Department of Physics and Astronomy
Rice University
6100 Main Street
Houston, TX 77005
Electronic Mail: cmj@rice.edu*

Christine Roark²

University of Iowa

¹Jansky Postdoctoral Fellow

^aVisiting Astronomer, McDonald Observatory, operated by The University of Texas at Austin

ABSTRACT

We present the results of a campaign to observe flares on the M dwarf flare star EV Lacertae over the course of two days in 2001 September, utilizing a combination of radio continuum, optical photometric and spectroscopic, ultraviolet spectroscopic, and X-ray spectroscopic observations, to characterize the multi-wavelength nature of flares from this active, single late-type star. We find flares in every wavelength region in which we observed. A large radio flare from the star was observed at both 3.6 and 6 cm, and is the most luminous example of a gyrosynchrotron flare yet observed on a dMe flare star. The radio flare can be explained as encompassing a large magnetic volume, comparable to the stellar disk, and involving trapped electrons which decay over timescales of hours. Flux enhancements at 6 cm accompanied by highly negatively circularly polarized emission ($\pi_c \rightarrow -100\%$) imply that a coherent emission mechanism is operating in the corona of EV Lac. There are numerous optical white-light flares, and yet no signature of emission line response from the chromosphere appears. Two small ultraviolet enhancements differ in the amount of nonthermal broadening present. There are numerous X-ray flares occurring throughout the observation, and an analysis of undispersed photons and grating events reveals no evidence for abundance variations. Higher temperatures are present during some flares, however the maximum temperature achieved varies from flare to flare. There is no evidence for density variations during any flare intervals. In the multi-wavelength context, the start of the intense radio flare is coincident with an impulsive optical U-band flare, to within one minute, and yet there is no signature of an X-ray response. There are other intervals of time where optical flaring and UV flaring is occurring, but these cannot be related to the contemporaneous X-ray flaring: the time-integrated luminosities do not match the instantaneous X-ray flare luminosity, as one would expect for the Neupert effect. We investigate the probability of chance occurrences of flares from disparate wavelength regions producing temporal coincidences, but find that not all the flare associations can be explained by a superposition of flares due to a high flaring rate. We caution against making causal associations of multi-wavelength flares based solely on temporal correlations for high flaring rate stars like EV Lac.

Subject headings: stars: activity, stars: coroneae, stars: late-type, radio continuum: stars, X-rays: stars, ultraviolet: stars

²NRAO REU Summer Student

1. Introduction

The study of extreme coronae, such as on M dwarf flare stars, allows an investigation into regimes of temperature, density, and activity not available from spatially detailed studies of our low-activity Sun. These stars are small, nearly (or fully) convective, and have intense magnetic fields covering a large majority of the stellar disk (Johns-Krull & Valenti 1996; Saar 1994). Despite their small size, dMe flare stars produce close to the maximum amount of coronal emission any star seems able to maintain — even in the quiescent state. Frequent large outbursts can increase the X-ray luminosity up to $\sim 20\%$ of the total stellar bolometric luminosity (Favata et al. 2000). Flares on these stars are fundamentally linked to magnetic processes occurring in their outer atmospheres, which involve the entire atmosphere and produce emission all across the electromagnetic spectrum.

EV Lac (dM4.5e) is a young disk population star at a distance of 5.1 pc; its young age comes from kinematics, based on infrared colors (Leggett 1992), $H\alpha$ observed to be in emission, rapid rotation, and flaring. It is the second brightest M dwarf X-ray source seen in the ROSAT All-Sky Survey, with a quiescent 0.1–2.4 keV flux of $\sim 4 \times 10^{-11}$ erg cm $^{-2}$ s $^{-1}$ (Hünsch et al. 1999). The quiescent X-ray luminosity is a significant fraction of the total bolometric luminosity ($\sim 0.2\%$). Its low mass ($0.35 M_{\odot}$) puts it near the dividing line for fully convective stars (Delfosse et al. 1998). EV Lac has very strong, 2.5–3.5 kG magnetic fields covering $> 50\%$ of the stellar surface (Johns-Krull & Valenti 1996; Saar 1994), so coronal phenomena are dominated by magnetic field interactions.

The optical variability of EV Lac is well known; Abdul-Aziz et al. (1995) detected 25 flares during 28 hours of five color photometric monitoring. Kodaira et al. (1976) saw a flare on EV Lac with an increase of 5.9 magnitudes in U band. The star is variable at radio wavelengths as well: White et al. (1989a) determined an upper limit of 0.3 mJy at 6 cm, while Caillault et al. (1988) detected the source at 1.0 mJy. White et al. (1989a) also found extremely polarized ($> 80\%$ left circularly polarized) emission at 20 cm, and Abdul-Aziz et al. (1995) observed bursts of decametric radiation associated with some of the optical flares reported. Pomerance et al. (1995) conducted coordinated IUE and EUVE observations, and recorded a factor of four enhancement in C IV emission preceding EUVE flare peaks. Earlier, Ambruster et al. (1986) measured a decrease in UV line fluxes of a factor of two over 1.5 hours, which they attributed to a major mass expulsion episode, similar to solar flare-related eruptive prominences.

EV Lac has been observed by many previous X-ray satellites and has shown extreme levels of variability. The types of flares have varied dramatically: from extremely short duration events that last a few minutes with an enhancement of ~ 10 over the quiescent count rate (Ambruster et al. 1994) to large events that can last up to 24 hours (Schmitt

1994; Sciortino et al. 1999) and peak at 300 times the quiescent count rate (Favata et al. 2000).

Based on its previous record for large and dramatic flare variability, we studied the multi-wavelength behavior of EV Lac with observations utilizing the *Chandra X-ray Observatory*, the *Hubble Space Telescope*, ground-based optical photometry and spectroscopy, and ground-based radio interferometry; these observations overlapped during two days in September 2001. The multi-wavelength span of observations allows a probe of the response of different layers of the atmosphere to a flare: radio wavelengths detail the role of nonthermal particles in flare dynamics; optical continuum photometric flare variations can be interpreted as emission from a black-body at temperatures of $\approx 10^4\text{K}$ (Hawley & Fisher 1992); optical spectroscopy probes chromospheric emission/absorption lines; ultraviolet spectroscopy details chromospheric and transition region temperatures; and X-ray spectroscopy describes thermal coronal plasma. The focus of this paper is an investigation of flare properties in the regions of the electromagnetic spectrum involved in the campaign, and the correlation of behaviors at different wavelengths; a companion paper (Osten et al., in prep.) will discuss the quiescent behavior.

2. Data Reduction

A time line of the observations is shown in Figure 1. The subsequent sections describe the individual programs.

2.1. VLA Observations

The star was observed with the NRAO¹ Very Large Array (VLA). The phase calibrator was 2255+420, and the flux density calibrator was 0137+331 (3C 48). On 20 September, the observations were performed simultaneously in two subarrays at 6 and 3.6 cm (4.9 and 8.4 GHz, respectively), to characterize the multi-frequency behavior of any flares that might occur during the Chandra observations. Processing of the data was done in AIPS. The field around EV Lac is crowded; there is a large radio galaxy ~ 2.7 arcminutes away, and numerous additional radio sources. We performed multi-field cleaning, taking advantage of the NRAO VLA Sky Survey (NVSS Condon et al. 1998) to locate possible bright radio sources

¹The National Radio Astronomy Observatory is a facility of the National Science Foundation operated under cooperative agreement by Associated Universities, Inc.

in the primary beam and sidelobes. After imaging the field, visibilities of sources not identified as EV Lac were removed, and the field was re-imaged. Subsequent analysis utilized the DFTPL program to extract the time variation of the source flux densities. The quantities measured are the total intensity, I , and the amount of circular polarization, π_c , defined as

$$\pi_c(\%) = \frac{V}{I} \times 100 \quad (2-1)$$

where I and V are the Stokes parameters for total intensity and circularly polarized flux, respectively. Left circular polarization (LCP) corresponds to $V < 0$; right circular polarization (RCP) corresponds to $V > 0$. The correction from International Atomic Time (IAT) to Universal Time Coordinated (UTC) was done using the values appropriate for 2001, $UTC = IAT - 31.8s$ (*Astronomical Almanac*).

2.2. Optical Observations

Observations were performed at the McDonald Observatory, using the 2.1m Otto Struve telescope and the 2.7m Harlan Smith telescope. The 2.1m telescope recorded photoelectric photometry in the UBVR Johnson-Cousins filters on 18, 19, and 20 September 2001, using a two-channel photometer. EV Lac was observed with the primary channel, while the second channel monitored the sky conditions with a U-band filter. Integrations in the UBVR filters were 3, 2, 1, and 1 seconds, respectively, including 0.161 seconds for filter rotation, resulting in a 7 second duty cycle. Sky measurements were made in the primary channel every 15–20 minutes. Extinction and photometric standard stars (Landolt 1973, 1992) were observed each night. We concentrate here on the night of 20 September, during which increasing cloud cover prevented absolute photometric accuracy. Instead, relative photometry of EV Lac was performed by dividing the temporal behavior of EV Lac in the primary channel with a field star in the second channel (done in the U filter only). We determined the relative variations outside of clouds or flares, normalized the count rates using this value, and converted to magnitudes using a quiescent U magnitude of 12.89, as determined by Andrews & Chugainov (1969). We used the zero point magnitude of Vega to convert magnitudes into flux densities. One large flare and a second smaller enhancement were detected in the relative photometry, along with smaller variations. For determination of flare energies, we used the U band luminosity of $5.01 \times 10^{28} \text{ erg s}^{-1}$ as determined from flux calibrated data of Gershberg & Chugainov (1969). Flare energies were determined by using the following formula:

$$E = L \times \sum_i \frac{I_f - I_q}{I_q} \Delta t \quad (2-2)$$

where E is the net flare energy, L is the quiescent luminosity in this filter, I_f is the flare intensity, I_q the quiescent intensity, Δt the time step, and the summation is over the data taken during the flare.

The 2.7m telescope was used in conjunction with the cross dispersed coude echelle spectrograph (Tull et al. 1995) to obtain high resolution optical spectroscopy with a time cadence minimum of 55 seconds (45 second exposures followed by ~ 10 seconds for readout and writing to disk; during cloudy periods exposures were lengthened to 60 or 90 seconds). The wavelength range was nominally 3750–9850 Å with small gaps between each of the 58 orders except in the far blue. Due to the relative faintness of EV Lac in the blue, and the short exposure times, the region blueward of H δ was usually too noisy for reliable measurements. The data were recorded on a 2048 \times 2048 Tektronix CCD which was binned 2 \times 2 to decrease readout time. As a result of this binning, the detector undersamples the spectrum. Spectra of a thorium-argon lamp are used to determine the wavelength solution of the instrument and to measure the resolution obtained during the run. The median FWHM of the 1210 thorium lines used in the wavelength solution is 1.16 pixels corresponding to a spectral resolution of $R \approx 55,000$. The wavelength solution was determined by fitting a two dimensional polynomial to $m\lambda$ as a function of detector column number and spectral order m . Spectra themselves are reduced in a standard way using software written in the IDL programming language and described by Hinkle et al. (2000). Briefly, the reductions include cosmic ray removal, dark current and background subtraction, and flat-fielding by a normalized exposure of an incandescent lamp. The continuum is normalized in each echelle order, enabling measurement of equivalent widths and line profile parameters. Variations in equivalent width of several prominent lines were determined during the flare.

2.3. Ultraviolet Observations

EV Lac was observed with the *Hubble Space Telescope Imaging Spectrograph* for 4 orbits on 20 September 2001, with a total data accumulation of about 10920 seconds. The data were obtained with the E140M grating, centered at 1425 Å in TIME-TAG mode using the FUV-MAMA detector and the 0.2x0.2 arcsecond aperture, to enable investigation of short time-scale variability at high spectral resolution. The wavelength range covered was 1140–1735 Å in 44 orders, with an approximate resolving power of $R = 45,800$.

We followed procedures described in Hawley et al. (2003) to determine variability and examine spectral variations. Spectra were extracted in 60 second intervals to search for large variability; the order location solution from the pipeline-processed data was used to

extract spectra and the corresponding wavelength solution was used. The background and spectral extraction widths were 7 pixels, and the background was fit by a second order polynomial; the background fit was then subtracted to obtain a net spectrum. Light curves were generated from the 60 second spectra by summing all counts, and subtracting the sum of the background; Poisson statistics were used to generate 1σ error bars.

2.4. Chandra Observations

The campaign centered around a 100 ks *Chandra* observation, which started 2001 September 19.8, and ended 2001 September 21.0. The observations were made using the High Energy Transmission Grating Spectrometer (HETGS) in conjunction with the ACIS-S detector array. The HETGS provides an image in zeroth-order light of the object as well as through two sets of gratings: the Medium-Energy Grating (MEG) covering the wavelength range 1.7–31 Å in first order and the High Energy Grating (HEG) covering the wavelength range 1.2–18.5 Å in first order, with almost twice the spectral resolution. The observation was taken in timed exposure mode, for which CCD events are accumulated every 3.24 s before being read out. This sets the minimum time resolution. *Chandra* data are recorded in terrestrial time (TT); we used the correction for 2001 to convert the data to universal time (UTC): $UTC = TT - 64.09s$ (*Astronomical Almanac*).

The *Chandra* data was processed using CIAO, Version 2.2, “threads”, or processing recipes, for different aspects of the data reduction. We eliminated bad aspect times and confirmed that the observation was not affected by ACIS “background flares”. We applied calibration products: the new ACIS chip pixel size (0.0239870 mm from 0.024 mm) and focal length (10070.0 mm from 10061.62) were updated in processing the ACIS events. Events with energies less than 300 eV and greater than 10,000 eV were excluded, as these are not well-calibrated; also excluded were events whose pulse-height invariant (PI) values were 0, 1, or 1024 (overflow/underflow values). Only ASCA grades 0, 2, 3, 4, 6 were kept. The data were resolved into spectral events using region filtering (rectangles around the MEG and HEG stripes), and a level 2 event file was generated. One of the CCD chips in the ACIS-S array (S4) suffered increased scatter (streaking) in the horizontal (CHIPY) direction, apparently caused by a flaw in the serial readout; a destreak filter was applied to remove these data.

We also extracted spectra corresponding to quiescence, and each flare, from the undispersed photon events. The source extraction region was a 3×3 pixel area centered on the location of 0th order, in which 95% of the undispersed photons lie. The background region was an annulus of 10 pixel radius, with the same center. Sensitivity and response matrices were generated for each time slice. We regrouped the CCD spectra to have a minimum of

25 photons in each spectral bin; 6 of the 9 flares had sufficient counts that we could perform spectral fits, and for a few of the longer duration flares, we attempted further time resolution by extracting spectra during the rise and decay phases.

We used custom IDL procedures to determine light curve variations and subsequent spectral analysis. The level 2 events file was filtered for MEG events falling within the spectral extraction window (± 0.1 mm in the cross-diffraction coordinate). The first 40 ks of the observation were unaffected by flares; we extracted a quiescent spectrum from this dataset. Degradation of the ACIS quantum efficiency (QE) at low energies (< 1 keV) has become a problem, due to the buildup of a contaminant on the ACIS optical blocking filter. We updated the sensitivity files to reflect this change.

3. Analysis of Individual Datasets

3.1. Radio

3.1.1. Large Flare

Following a long span of small modulations (peaks in intensity ≤ 2 mJy) during the VLA observation on 20 September, a large flare occurs toward the end of the 11 hour track at both 3.6 and 6 cm in Figure 2, with a peak in flux of ~ 61 mJy at 3.6 cm ($L_R \sim 1.9 \times 10^{15}$ erg s $^{-1}$ Hz $^{-1}$). Figure 2 also shows the variations in spectral index and circularly polarized flux during the flare decay. This flare represents a maximum enhancement of ~ 150 over the preflare values; previous centimeter-wavelength radio observations had revealed evidence of small variations (White et al. 1989a; Caillault et al. 1988) on EV Lac, but the maximum flux density recorded was only 1.0 mJy. We consider the large outburst recorded at 3.6 and 6 cm to be a truly unusual event, with a long (> 3 hr) timescale, large (30–60 mJy) peak radio luminosity, yet small ($< 20\%$) circular polarization.

The spectral indices start out very steep, and decline approximately linearly. Panel (c) shows a close-up of the spectral index behavior: for ≈ 40 seconds before the 3.6 cm peak the spectral index is roughly constant, at $\alpha \sim 1.4$. Such large spectral indices during the initial phases of the flare indicate large optical depths in the flaring plasma; both frequencies are likely optically thick. At late stages in the flare the spectral index has reached a value of $\alpha \sim -1.6$ and the radiation at 3.6 cm is likely optically thin. The decline in flux is not characterized by a single exponential decay at either frequency; instead, the timescale τ over which the radiation decays exponentially (flux $\propto \exp(-(t - t_0)/\tau)$; t_0 is time of peak flux) progressively lengthens during the flare decay. Table 1 lists the exponential decay timescales

at both frequencies during various stages of the flare decay. The 3.6 cm flux decays at a faster rate (smaller decay timescale) than the 6 cm flux, but the increase in the timescale as the decay proceeds occurs at both frequencies.

The interpretation of this flare is complicated by optical depth effects early in the flare, when electron acceleration, injection into a flare loop, and particle trapping are most likely to occur. In contrast, the late stages of the flare appear to be consistent with optically thin emission at the higher frequency (3.6 cm, or 8.4 GHz). We interpret the variations at both frequencies under the assumption that the emission mechanism is gyrosynchrotron radiation from a nonthermal population of mildly relativistic electrons, whose distribution with energy is described by $N(E) \propto E^{-\delta}$ (see Dulk 1985). The spectral indices obtained during the flare rise, peak and initial decay, however, are not consistent with the range expected from a homogeneous optically thick source (2.5–3.1 for δ between 2 and 7; Dulk 1985), and therefore it is probable that multiple sources with different magnetic field strengths (perhaps an arcade of loops) are contributing to the observed radio emission. It is difficult to separate the temporal behavior of the emission (number and distribution of accelerated electrons, changing magnetic field strengths) from temporal change of the source size; both are conflated in measurements of total flux density.

We investigated some of the key parameters which control the amount of radio emission radiated during the flare. We assume that the emission at both 3.6 and 6 cm is optically thick, and originates from an inhomogeneous magnetic field with a large dipole configuration, or $B(r) = B_0(r/r_0)^{-3}$, where $B(r)$ describes the magnetic field strength distribution as a function of radius. The assumption of optically thick emission allows us to equate the brightness temperature with the effective temperature of the plasma, and implies that the emission is coming from a layer where the observed frequency is the peak frequency, i.e., where $\tau = 1$. We assume that the distribution of nonthermal electrons remains a power-law with fixed index $\delta = 3$ through the flare decay. Using the analytic expressions in Dulk (1985), the flux density can be expressed as

$$S_\nu = 2k_B T_B \Omega \frac{\nu^2}{c^2} = 2k_B T_{\text{eff}} \frac{\nu^2}{c^2} \frac{\pi r_s^2}{D^2} \quad (3-1)$$

where S_ν is the flux density, k_B is Boltzmann’s constant, T_B is the brightness temperature, T_{eff} is the effective temperature, ν is the observing frequency, Ω is the solid angle subtended by the source, r_s is the source size and D is the distance to the source. Adding in equation 37 of Dulk (1985) describing the dependence of effective temperature on δ , ν , B , and angle θ between magnetic field and line of sight, we solve for the changing source size as a function of time at the two radio frequencies, assuming that r_0 is the stellar radius, B_0 is ≈ 3000 G, $\delta = 3$, $\theta=60^\circ$. The small spectral indices in quiescence indicate a shallow number distribution

with energy, compatible with $\delta = 2$ or 3 , and we choose $\delta = 3$. This is also compatible with previous models for nonthermal stellar radio emission, which find that flat spectral energy distributions are better able to reproduce observed spectral energy distributions (White et al. 1989b). The dependence on angle θ is not steep, and we choose an angle θ of 60° as representative. Figure 3 plots the variation of the source size, magnetic field strength in the source, and effective temperature for the two radio frequencies during the decay of the large flare. Once the magnetic field strength in the source is known, the total number density of nonthermal electrons above a cutoff energy E_0 , can be calculated, using equation (39) of Dulk (1985) (in these calculations $E_0 = 10$ keV is assumed); this quantity is also plotted in Figure 3. Note that the source sizes are larger than or comparable to the stellar radius $R_\star \approx 2 r_{10}$ cm. The minimum magnetic field strengths at the flare peak are 60 and 110 Gauss, at 6 and 3.6 cm respectively, and maximum effective temperatures $\sim 3.4 \times 10^9$ K. The higher frequency indicates a larger field strength at all times due to the larger gyrolayers being sampled. The magnetic field strength increases with time during the flare decay, a consequence of the decreasing source size, as the location of optical depth unity moves closer to the stellar surface. These values are consistent with values previously determined from e.g. VLBA studies of M dwarf coronae (Benz et al. 1998).

The major energy loss mechanisms for accelerated electrons during solar flares are Coulomb collisions from electrons caught in a magnetic trap, and precipitation from the trap into the chromosphere via scattering into a loss cone (so-called trap plus precipitation models; Melrose & Brown 1976). Coulomb collisions preferentially deplete low energy electrons compared to high energy electrons; the timescale for radiative loss goes as $E^{3/2}$, and the observed flare variation at each frequency is qualitatively consistent with the hypothesis that Coulomb collisions dominate during the decay phase, as the timescales grow larger during the decay. The collisional deflection time is approximated in the weak diffusion limit by

$$\tau^{\text{defl}} = 9.5 \times 10^7 \left(\frac{E_{\text{keV}}^{3/2}}{n_e} \right) \left(\frac{20}{\ln[8 \times 10^6 T_e / n_e^{1/2}]} \right) \text{ s} \quad (3-2)$$

(Benz 2002), where n_e and T_e are the ambient trap particle density and temperature, respectively; and E_{keV} is the energy of the accelerated particle in units of keV. By analogy with solar flare behavior, the observed decay timescales for the flare on EV Lac listed in Table 1 are consistent with very energetic electrons, or a remarkably low trap density, or a combination of the two. A trap density of $n_e \sim 10^8 \text{ cm}^{-3}$ and thermal electron temperature of $T_e \sim 10^7$ K are consistent with the observed decay times and with particles of ≈ 100 – 400 keV in energy. During the flare decay, then, one expects that the low energy particles will lose energy and precipitate from the trap, resulting in a hardening of the electron distribution with energy. The toy model for magnetic field inhomogeneities described above assumes that

the number distribution with energy has a fixed index, and only the total number density above a cutoff energy E_0 decreases. The depletion of low energy electrons from the trap could be simulated in the model by a corresponding increase in the cutoff energy in the electron density distribution with energy. The ratio of nonthermal electron density to thermal electron density in the trap implied by the model is very high, $\sim 10^{-2}$ at the beginning of the flare decay.

3.1.2. *Small Flares*

Several smaller amplitude flares are also evident in the data, particularly at 6 cm (Figure 4), accompanied by large amounts of circularly polarized flux. Computations of “pre-flare” values of average flux and polarization were determined by limiting the time range to 03:30:00 – 08:25:00, to avoid any of this smaller scale variability (although it is still apparent at 3.6 cm). The average preflare fluxes at 3.6 and 6 cm are 0.41 ± 0.02 and 0.65 ± 0.03 mJy, respectively, and the average circular polarization (average V flux divided by average I flux) at 3.6 and 6 cm is $-22 \pm 5\%$ and $-22 \pm 5\%$, respectively. There are two events at 6 cm which reach 100% circular polarization, with no apparent correspondence at 3.6 cm. These events occur in both intermediate frequencies used in the 6 cm observations, spanning 4810–4910 MHz. The lack of corresponding variations at 3.6 cm constrains the bandwidth of the event to be $100 \text{ MHz} \leq \Delta\nu \leq 3500 \text{ MHz}$. The peak amplitudes of a few mJy are rather small, implying that the peak radio luminosity is $6.2 \times 10^{13} \text{ erg s}^{-1} \text{ Hz}^{-1}$. This behavior is very reminiscent of radio bursts with large amounts of circular polarization seen on other active M dwarfs, which have accompanying large brightness temperatures (generally $> 10^{13} \text{ K}$) and short durations, although an event on the dMe star Proxima Centauri reported by Slee et al. (2003) had 100% right circular polarization lasting for days.

The two highly polarized events early in the observation are relatively long-lasting, having durations of ~ 1 hour each. The large amounts of circular polarization argue for a relatively localized phenomenon, due to the large brightness temperatures needed ($\geq 10^{13} \text{ K}$) to generate extreme circular polarization levels (usually a coherent process is needed); the source size can be calculated as

$$r_{10} = \frac{d_{pc}}{8.7} \left(\frac{5GHz}{\nu} \right) \left(\frac{S_\nu}{100mJy} \right)^{1/2} \left(\frac{4.8 \times 10^{10}}{T_b} \right)^{1/2} \quad (3-3)$$

where r_{10} is the source size in 10^{10} cm , d_{pc} is the distance to the source in parsecs, ν is the observing frequency, S_ν the flux density, and T_b the brightness temperature; using a lower limit of 10^{13} K for the brightness temperature requires r_{10} to be less than 6×10^{-3} , or about

0.1% of the stellar diameter.

3.2. Optical

Two flares are evident in the U band light curve depicted in Figure 1. The first is an enhancement of only 0.68 magnitudes, lasting ~ 268 seconds (peak at 20 September 04:04:34 UT), while the other has a peak of 3.3 magnitudes above the quiescent value and lasts for about 420 seconds (peak at 20 September 08:29:31 UT). Using the formula described in §2.2, we estimate the flare energies to be 2.6×10^{30} ergs and 5.2×10^{31} ergs for the two flares, respectively. The existence of clouds prior to and during the larger flare makes precise determination of the flux variations difficult, but there appear to be smaller enhancements between 06:00 and 08:00 UT. We are able to determine relative flux variations in the U-band filter only because the second photometer channel also had a U-band filter in it monitoring another star; the variations in BVR cannot be disentangled from cloud variations, but we do clearly see the larger flare in all the colors.

We also investigated the variations of equivalent widths of chromospheric lines — the data are displayed in Figure 5. The presence of clouds reduced the flux, thereby making continuum normalization difficult (due to the decreased count rate) and adding systematic error to the resultant equivalent width calculations; for this reason we excluded spectral time slices based on low signal-to-noise of the spectral order (generally $\text{SNR} < 10$). There is some evidence for variation of $\text{H}\alpha$ during the flare decay, however due to the variable cloud coverage it is not possible to quantify accurately how much variation took place. We note that previous studies of EV Lac (Baranovskii et al. 2001a,b) determined a range of $\text{H}\alpha$ equivalent widths of 3.5–5.3 Å, and $\text{H}\beta$ equivalent widths of 4.4–5.0 Å during quiescent periods; during “active states” the range of equivalent widths they observed was 4.7–10.6 Å and 10.2–20.9 Å, respectively. As shown in Figure 5, our equivalent width measurements span ~ 3 –4 Å. There was an impulsive U-band flare during our observations around 08:29:31 UT, and we observe some variation of equivalent width in $\text{H}\alpha$ and $\text{H}\beta$, but the existence of similarly large variations one hour later (when no photometric flare indicators are present) make the flare interpretation problematic. Hawley et al. (2003) noted from studies of flares on the M dwarf flare star AD Leo that optical chromospheric lines have a long gradual phase, compared to the impulsive continuum variations, and if such events are common to flare stars, we should have had an increased probability of observing enhanced equivalent widths during the flare.

3.3. Ultraviolet

Two small enhancements can be seen in the UV light curves in Figure 1, in orbits 1 and 3 of the four HST orbits in which data were taken. The peaks were reached at 16:53:46 and 19:48:00, represent enhancements of ~ 1.5 (1.8) times the nearby count rates, and last for only about 4 (5) minutes, respectively. The total UV energy released during the two flares was estimated by subtracting from each the quiescent spectrum, and integrating from 1270–1750Å; the first flare radiated 1.4×10^{29} erg, the second 5.0×10^{29} erg. We attempted to determine spectral variations during the events. Previous analyses of spectral characteristics of ultraviolet flares on active stars revealed a variety of phenomena, from downflows with velocities up to 1800 km s^{-1} (Bookbinder et al. 1992) to broadening of Si IV line profiles with widths of up to 500 km s^{-1} (Linsky & Wood 1994), to blue-ward enhancement of continuum emission during flares (Robinson et al. 2001). However, due to the low enhancement above the non-varying count rate, and short time duration of these events, the signal-to-noise of the 60-second flare spectra was not high enough to determine any of these reliably.

We next co-added all the 60 second spectra which occurred during flares, to investigate gross flare-quiescence differences and flare-flare differences. An examination of the strongest features during the two flares, in comparison with quiescent line profile shapes, is given in Figure 6. Our fitting routine (based on Hawley et al. 2003) estimates the surrounding continuum level, and performs single and double-Gaussian line-profile fitting to the brightest lines in the flare spectra; the results are listed in Table 2.

A feature common to transition region emission line profiles from active stars is extended wings in the line profile (Wood et al. 1996) which are fit better by two Gaussian profiles than a single Gaussian. For the quiescent spectrum, this is the case; however, the flare spectral profiles did not show any statistically better fit using two Gaussians than one (due partly to signal-to-noise constraints) and therefore we fit only a single Gaussian profile to the features in the flare spectra. The flare profiles analyzed by Linsky & Wood (1994) on the dMe flare star AU Mic, while showing remarkable amounts of broadening, also were consistent with single Gaussian shapes. None of the lines analyzed here shows conclusive evidence for bulk plasma motions during either flare. Only for the narrow component of the quiescent spectrum does there appear to be a deviation from zero, and it appears to be temperature-dependent, with the magnitude of the blueshifts increasing towards higher temperatures.

We investigated evidence for nonthermal motions in the line profiles, presumed to have a Gaussian distribution, and present in the line profile widths above the expected thermal widths of the emission lines. The turbulent velocities deduced for the two flare segments are comparable to that deduced from the narrow component of the quiescent lines, and appears to be temperature-dependent, in that temperatures below 10^5K show evidence of excess

line widths, while the highest temperature line examined (N V λ 1238) shows no turbulent broadening.

The second flare has line widths almost twice those of the first flare, and the narrow component of the quiescent features, although the broad component to the quiescent features is still largest. The flux enhancements of the two flares are similar for the high temperature lines probed in Table 2, with the exception of Si III λ 1206, for which the second flare has three times the flux of the first.

3.4. X-ray

Numerous X-ray flares are evident in the light curve of Figure 7, shown binned at 300 seconds. At least nine flares with a peak enhancement of $> 60\%$ over the surrounding count rate are noticeable, and they are clumped in time, occurring during the last 60 ks of the observation. The first 40 ks appear to be characterized by lower-level modulations which may be evidence of smaller amplitude variability. The average count rate in the first 40 ks is 0.17 ± 0.03 ct s $^{-1}$, and the X-ray luminosity during this time from dispersed spectra (1.8–26 Å) is 1.8×10^{28} erg s $^{-1}$. We estimate the lower limit of the X-ray flaring rate to be 0.32 flares hr $^{-1}$, using the nine individual flares noted in Figure 7. Several flares appeared extremely impulsive, and we investigated variations by extracting a light curve with a finer time grid of 60 seconds. Panels (b) and (c) of Figure 7 detail flares with the largest enhancements above the nonflaring count rate. We determined the time and count rate corresponding to the flare peak using the 60 second light curve for each of the nine flares, and extracted spectra (both grating and 0th order) corresponding to each of these flares. The number of X-ray photons extracted from each flare was not enough to assemble a dispersed MEG spectrum with good enough statistics to perform an investigation of flare-to-flare variations. We used the MEG data from each flare to estimate the excess energy radiated during each flare, and these numbers, together with count rates and durations, are tabulated in Table 3.

3.4.1. Analysis of Zeroth Order Spectra

The location of the undispersed light falls on ACIS chip S3, which has FWHM energy resolution 100 – 200 eV between 1 keV and 8 keV; in addition, the spectrum suffers from pileup effects, due to the detection of two soft photons as one hard photon with the combined energy of the two actual photons. This can cause an artificial hardening of the apparent X-ray spectrum. Since 95% of the 0th order photons fall within a central 3 \times 3 pixel area,

and EV Lac has a low count rate (~ 0.17 counts s^{-1} during quiescence), it is not feasible to examine the 0th order time-resolved spectra outside of the piled-up regions. A correction for the effect of pile-up has been implemented in Sherpa and XSPEC using the model of Davis (2001) to correct for grade migration. We model the zeroth order spectra using as multiplicative models the pileup and interstellar absorption, and additive models two discrete temperature APEC models within XSPEC (using the abundances of Anders & Grevesse 1989). Although Sciortino et al. (1999) used an interstellar hydrogen column density of $\sim 10^{19} \text{ cm}^{-2}$ in analysis of ROSAT and BeppoSAX observations, we kept N_H fixed to 10^{18} cm^{-2} in analyzing the ACIS spectra, as *EUVE* spectra constrain it to be lower than a few times 10^{18} cm^{-2} (Osten et al, in prep.).

Table 4 lists the spectral quantities derived from quiescence, as well as six of the nine individual flares, and Figure 8 displays the spectra and model fits. The lowest temperature component in all cases is consistent with a value of about 4 MK, while the high temperature component varies from 9 to 30 MK. Flare 8 is the interval which shows the hottest plasma temperature. The global abundance, Z , appears to be low in all spectra, but shows no significant variations; this is limited, however, by the large error bars for some flare spectra, which prevent determining variations of factors of three or less. For flares 8 and 9, no convergence could be found for a simple global metallicity scaling, and instead we decoupled the abundances and solved for O, Ne, Mg, and Fe separately. There is again no evidence for abundance variations, within the large error bars for the derived values.

For the three longest lasting flares (1, 8 and 9) we extracted spectra corresponding to the rise and decay phase, separately, to investigate possible intra-flare plasma changes. The results are also listed in Table 4 and displayed in the right panel of Figure 8. There were only significant counts during the decay phases, and the flare decay spectra show a consistent pattern, being well-described by a two-temperature fit, the lower temperature corresponding to values derived from quiescent intervals, and the higher temperature between 11 and 20 MK; the global abundance is similarly low in all three cases. During the decay of Flare 1 we found it necessary to fix the temperature and emission measure of the cooler component, allowing the higher temperature and emission measure, and global metallicity, to vary. There is no evidence of dramatic abundance variations, as have been found from studies of other stellar flares. For Flare 1, there is no significant difference between the temperatures derived from the entire flare and those derived from the decay, suggesting that the rise phase of the flare was not hot enough (or did not contain enough material) to affect the integrated flare spectrum. For Flares 8 and 9, however, the hotter temperature component during the decay phase is smaller than obtained from the integrated flare spectra.

We attempted to fit simplistic, one temperature models with pileup to the few counts in

the rise phase spectra. The spectra during the rise phases are remarkably different from each other (and from the decay spectra); the rise phase of flare 8 implies very hot temperatures, while the rise of flare 1 shows no significant departure from the quiescent temperatures, and the rise of flare 9 shows a modest (factor of two) increase. The abundances of the rise phase spectra had to be treated differently in each case, in order to get a convergent fit. For the rise phase spectra of flare 1, we decoupled the Ne abundance from the others, finding somewhat enhanced Ne; however, the large error bars swamp this. For the rise phase spectra of flare 8, we fixed the abundance at solar due to the low number of spectral bins. For the rise phase spectra of flare 9, we allowed the global abundance to vary freely, finding generally low values. For these spectra with poor spectral resolution and S/N, it is difficult to conclude whether these fits reveal evidence for abundance anomalies.

3.4.2. *Analysis of Grating Spectra*

The number of X-ray photons extracted from each flare was not enough to assemble a dispersed MEG spectrum with good enough statistics to perform an investigation of flare-to-flare variations. Instead, we co-added time intervals of small flares (flares 3–6 and 9) and large flares (1,2,7,8) to see if there was any discernible spectral difference between small amplitude events and larger amplitude events. Even with these broad groupings the number of counts in the accumulated spectra is not enough to perform a time-resolved differential emission measure (DEM) analysis, so we adopted a different approach. One of the X-ray signatures of stellar flares is the creation of hot plasma, generally $T > 10$ MK, during flares. At these high temperatures, there are relatively few atomic transitions, mostly arising from transitions in hydrogenic and helium-like ions from high Z elements (Si, S, Ca, Fe). A major contributor to the X-ray emission at such temperatures is continuum emission due to free-free and free-bound processes. High spectral resolution analyses of active M star coronae reveal an underabundance in elements whose first ionization potential is less than 10 eV relative to solar photospheric abundances (van den Besselaar et al. 2003). Abundances often increase during flares (Favata et al. 2000), although this is not observed for all flares (Huenemoerder et al. 2001). We investigated the spectra of quiescence, small flares, and large flares, looking for signatures of high temperature plasma through emission lines and continuum emission, as well as possibly elevated abundance levels during flares. A detailed DEM analysis of the composite X-ray spectra, along with the STIS spectrum and other wavelength regions, is presented in a companion paper (Osten et al., in prep.).

Figure 9 displays the continuum X-ray spectra during three different intervals, corresponding to quiescence, large enhancement flares, and smaller flares. The wavelength regions

used were determined from the Astrophysical Plasma Emission Code (APEC) line lists (Smith et al. 2001) as comprising only weak emission lines (peak emissivities less than 10^{-18} photons $\text{cm}^{-2} \text{s}^{-1}$). Under the assumption that most of the flux arises from continuum emission, we binned these spectral regions to estimate the shape and amount of continuum emission. Our previous analyses of Chandra *HETGS* data (Osten et al. 2003) have shown that this is a good approximation. The continuum level is elevated in both flare intervals, compared to quiescence, and the flare continuum enhancement is larger for the spectrum comprised of large flares. The continuum from large flares is about seven times larger than quiescence; the continuum from smaller flares also shows an increase of ~ 2.5 compared to the average quiescent continuum shape. There is no discernible difference in the shape of the continuum spectra for large flares and small flares, modulo the large error bars at short wavelengths. Figure 9 illustrates the distribution of continuum flux from an isothermal plasma with a temperature of 12 MK for the three different observed activity states, where the amount of material is varied to match the peak observed flux; we cannot constrain the presence of temperatures hotter than this amount using the continuum. A large temperature difference would show up as a change in the peak of the continuum spectrum, moving towards shorter wavelengths for hotter temperatures. The gap in continuum from 8–17 Å is due to the large number of iron L shell lines contributing emission in this region; it is not possible to measure the underlying continuum emission in this region directly.

We also examined individual strong emission lines to gauge their variations through intervals of differing activity. Table 5 lists the dominant hydrogenic and helium-like transitions of Si, Mg, Ne, and O. The fluxes were determined from fits to the MEG spectra after subtraction of an estimate of continuum emission (shown in Figure 9). Gaussian line profiles of fixed width (equal to the instrumental resolution of 0.023 Å for MEG) were used to determine the wavelength of line center as well as total line flux; errors were estimated using the formulations of Lenz & Ayres (1992). Line fluxes for quiescence, large flares, and small flares are listed in Table 5. The large flares generally also had the largest enhancements in line fluxes. Despite the fact that a detailed differential emission measure analysis cannot be done on the time-resolved data, we examined evidence for temperature and abundance variations by formulating line ratios of (1) hydrogenic and helium-like transitions from the same element, which should have a temperature dependence but no abundance dependence; and (2) different elements with overlapping temperature dependences. These are given in Tables 6 and 7. The theoretical energy flux ratios for the corresponding emissivities from APEC, using solar abundances of Grevesse & Sauval (1998, 1999), are also listed.

Table 6 lists the observed values of temperature-sensitive emission line ratios, along with the inferred temperatures and errors derived from theoretical emissivity curves for the transitions listed. The four ratios indicate that a range of temperatures is present in the

coronal plasma during all three temporal segments. For the large flares, the ratios give evidence of hotter plasma compared to quiescent conditions; only a modest enhancement in the temperatures is deduced during the small flares. This may be because the contribution from quiescent emission dominates in the small flares compared to the large flares. The line ratios are more sensitive to small increases in the maximum temperature present, but the continuum results are not inconsistent with the temperature changes deduced from line ratios. This is consistent with previous analyses which indicate hotter temperatures during larger flares (Feldman et al. 1995). The largest temperature enhancements during the flare intervals occur for line ratios with the highest temperature sensitivity, which is consistent with previous observations showing the creation of additional high temperature material during flares compared to quiescence (Osten et al. 2003).

Five different ratios which give constraints on coronal abundances were formed, and are listed in Table 7. The ratios were classified according to first ionization potential (FIP) of the elements: low FIP is less than 10 eV, and high FIP is greater than 10 eV. Observations of the solar corona show evidence for a FIP-dependent abundance bias, with low FIP elements preferentially enhanced over high FIP elements (Feldman & Laming 2000), while recent observations of active stellar coronae show an inverse FIP bias (van den Besselaar et al. 2003). While our observations can only constrain abundance ratios, not overall abundances, the pattern revealed by the ratios of fluxes from low FIP to high FIP elements is consistent with an enhancement of Ne and O (high FIP elements) over the abundances of Fe, Mg, and Si (all low FIP elements). The ratios are generally consistent across the time slices, except for a slight decrease in the Fe/Ne and Mg/Ne ratios during the two flares, which is consistent with a slight enhancement of the Ne abundance. During the time interval encompassing small flares, there is a noticeable increase in the Si/Mg abundance ratio compared both to quiescence and larger flares.

We also examined evidence for variation in electron densities during the spectra comprised of large and small flares, respectively, from quiescent conditions. The intercombination lines i and forbidden lines f of helium-like triplets of O VII, Ne IX, Mg XI, and Si XIII can be used to estimate the electron density at temperatures ranging from 2 to 15 MK. The energy flux ratios f/i are plotted in Figure 9 at the temperature of peak emissivity for the ion; the flare intervals show no significant variation from the quiescent points.

4. Multi-Wavelength Correlations

There are two temporal regions of overlap between the five telescopes involved in the campaign on 20 September 2001: VLA, McDonald 2.1, 2.7m telescopes, and *Chandra* overlap

from 02:00–12:00 UT, and *Chandra* and *HST* overlap from 16:00–24:00 UT.

Figure 10 illustrates the behavior from 02:00 until 08:00 during the first period of overlap. From 02:00–06:00 there is a small event around 03:04, and a moderate optical flare at 04:04. The X-ray variations occur with an average and standard deviation of 0.17 ± 0.03 counts s^{-1} , which we identify as the “quiescent” count rate. There are a few small radio (3.6 cm) enhancements, which do not appear to be correlated temporally with any of the optical events. As mentioned in §3.1, the 6 cm variations from roughly 00:30 until 04:00 are characterized by large amounts of circular polarization, yet there is no multi-wavelength context for these variations as no corresponding variability is evident at X-ray or optical wavelengths. This is generally consistent with previous determinations of a lack of correlation between coherent flare signatures and X-ray/optical flare signatures (Kundu et al. 1988; Gagne et al. 1998).

Figure 11 shows the behavior from 08:00–12:00 UT during the first period of overlap. The first impulsive X-ray flare occurred during an interruption in optical coverage, and there are no apparent radio variations during this event. There are subsequent small X-ray enhancements, but any possible corresponding variations in the optical are obscured by heavy cloud coverage, and in the radio by the decay of a large event. Figure 12 illustrates the X-ray and UV variations during the time of overlap of *Chandra* and *HST*. The two small UV flares appear to occur during periods of flaring X-ray activity.

4.1. Large Radio/Optical Flare

There is a close temporal association between the large U band flare and the radio flare displayed in Figure 11, yet no indication of an accompanying X-ray flare exists. The optical flare peaks ≈ 20 minutes after the impulsive X-ray event, too far apart in time to causally connect under any realistic length scales or velocities. The inset of Figure 11 shows a close-up of the U band and radio flares; all three flares appear to start at the same time, within the 10 second temporal sampling of the radio data. The U band peak precedes the 3.6 cm peak by roughly 54 seconds. Hawley et al. (2003) used as a criterion to determine the changeover from impulsive to gradual phase of the flare the time when the first derivative of the U band light curves changes sign following the flare peak. By this definition, the impulsive phase ends approximately 7 seconds after the U band peak and most of the radio flare at 3.6 and 6 cm occurs during the gradual phase of the flare.

Solar white light flares are rare, but seem to show evidence of association with hard X-ray and microwave bursts, suggesting that the optical continuum emission is at least partly

due to the acceleration of electrons (Neidig 1989). Our observations of a temporal association between an energetic optical stellar flare and a large microwave flare seem to support this hypothesis for the outer atmosphere of EV Lac. Neidig & Kane (1993) observed similar timescales for the hard X-ray (50 keV) and white light solar flare emissions, with the hard X-ray emission generally occurring first, by ≈ 8 seconds. If we assume that the optical continuum emission is a response to the bombardment of EV Lac’s lower atmosphere by accelerated particles, and the microwave emission is gyrosynchrotron emission from accelerated electrons caught in a magnetic trap, then the time delay of the gyrosynchrotron emission could be due to the kinematics of the particle injection and trapping. An anisotropic pitch angle distribution of the injected electrons can cause a significant delay between the time profile of injected electrons and that of trapped electrons, as Lee & Gary (2000) demonstrated for solar flares. Without more constraints, we cannot say conclusively that this is the case for the flare on EV Lac, but the evidence is suggestive.

While we do not have conclusive multi-band optical photometry during the flare due to cloudy conditions, we assume that the characteristics of this flare are similar to other well-studied flares on similar stars (Hawley et al. 2003); namely, that the rise in optical continuum emission is due to black-body radiation at temperatures of about 10^4K , covering a small area fraction ($\sim \text{few} \times 10^{-4}$) of the stellar disk. The temporal association between the optical and radio flares suggests that the two are causally related. The radio flux density measures the brightness temperature and source size, both of which are unknown. We use the optical area filling factor derived from other flare studies as appropriate for this flare, and assume that the source size expands from the photosphere (where the optical emission originates) to the corona (where the radio emission originates). We assume that the photospheric magnetic field involved in the flare is of the same order as deduced from observations of Johns-Krull & Valenti (1996), namely, 2.5–3.5 kG, and constrain the coronal magnetic field by the harmonic numbers appropriate for gyrosynchrotron emission ($\nu = s\nu_B$, $\nu_B = 2.8 \times 10^6 \text{B Hz}$, $s = 10 - 100$, and $\nu = 4.9, 8.4 \text{ GHz}$). Then we can derive an approximate relation for the size of the radio source, using potential field configuration and conservation of magnetic flux. The area expansion between photosphere and corona should then be

$$\Gamma = \frac{B_{phot}^{1/2}}{B_{cor}^{1/2}} = \frac{A_{cor}^{1/2}}{A_{phot}^{1/2}} \quad (4-1)$$

where B_{phot} is the photospheric magnetic field strength, B_{cor} is the coronal magnetic field strength, A_{cor} is the cross-sectional area which encompasses the coronal magnetic field, and A_{phot} is the cross-sectional area which encompasses the photospheric magnetic field. Using the above estimates of B_{phot} and B_{cor} gives an estimate of Γ ranging from 4–10. If $A = x \times A_\star$, and x_{phot} is $\sim 10^{-4}$, then x_{cor} should be 10^{-3} – 10^{-2} . (We note in passing that results from solar

studies have indicated much smaller area expansion factors, Γ of order 1.3; Klimchuk 2000; Watko & Klimchuk 2000). For the apparently optically thick conditions at the flare start, the brightness temperature can be equated with the effective temperature of the electrons; we use the 6 cm fluxes as they appear to be optically thick during all of the flare decay. The implied brightness temperatures are $\sim 10^{12}$ K, and the average energy of the accelerated electrons is quite high, ~ 90 MeV. However, VLBA studies of dMe stellar coronae show (Benz et al. 1998) a source size several times the stellar radius, and T_b of a few $\times 10^8$ K, with loop top field strengths > 15 G. In order to obtain a brightness temperature within the expected range for gyrosynchrotron emission at centimeter wavelengths, $T_b \approx 10^8$ – 10^{10} K, the area filling factor for the radio source must be of order unity; i.e. the radio source must be the size of the star itself. The average accelerated electron energy would then be in the range several tens – several hundreds of keV. This is consistent with the results from §3.1.1.

The estimate of the energy of the accelerated particles becomes important in quantifying the ambient density of the magnetic trap. Following equation 3-2, electrons with average energy ~ 90 MeV imply high ambient electron densities ($n_e \sim 10^{12}$ cm $^{-3}$) to explain the observed decay timescales as trapping effects. These large densities would imply substantial amounts of free-free absorption, and make such an interpretation problematic. For brightness temperatures compatible with the large observed VLBA source sizes, and energies \sim few hundred keV, a much lower ambient electron density is required, $n_e \approx 10^8$ cm $^{-3}$. Without an actual measurement of the radio source size, both solutions are possible, but the latter seems more plausible.

4.2. The Breakdown of the Neupert Effect

The coordination of so many telescopes spanning different wavebands offers a unique opportunity to test current understanding of stellar flares. Within the standard framework of solar flares (Dennis & Zarro 1993), the optical and radio emission probe the energetics of accelerated electrons. Solar (and stellar) ultraviolet emission enhancements are associated with nonthermal energy deposition, and an increase in thermal coronal radiation occurs as result of chromospheric evaporation, in which chromospheric plasma, having been heated to coronal temperatures by the deposition of nonthermal energy from accelerated particles, undergoes a radiative instability and fills up coronal loops to radiate at EUV/X-ray wavelengths. This gives rise to an observed relationship between thermal coronal emission and radio/hard X-ray nonthermal emission, with the timescale for thermal coronal radiation being proportional to that for the increase in nonthermal energy deposition. Despite the success with which previous authors found evidence of the Neupert effect in dMe flare star coronae

(Hawley et al. 1995; Güdel et al. 1996; Güdel et al. 2002; Hawley et al. 2003), we find a complete breakdown between the action of nonthermal particles and thermal response, on numerous occasions.

A gradual X-ray flare is evident during the interval 06:00–08:00 in Figure 10, along with several small optical flares. There is no noticeable response at radio wavelengths to either the optical or X-ray variations. We investigated the luminosity variations in the optical light curve to determine if their time variations were consistent with a Neupert effect interpretation. The models of Hawley & Fisher (1992) showed that the optical stellar flare continuum emission can serve as a proxy for hard X-ray nonthermal emission, which arises due to the particle acceleration event at the beginning of the flare. Hawley et al. (1995) and Hawley et al. (2003) found a correspondence between the time integral of the U-band luminosity and the instantaneous EUV luminosity, for flares on another active flare star (AD Leo). Figure 13 illustrates the X-ray and optical data during the time of the first X-ray flare. Because of non-photometric conditions, we attempted to correct for the influence of clouds by setting the luminosity during apparent quiet times equal to the U-band luminosity of Gershberg & Chugainov (1969), 5.01×10^{28} erg s⁻¹. During intervals affected by clouds (e.g. 7:06–8:12 UT), we fit the temporal variations with a second order polynomial and divided the observed variations by this fit, normalizing to the quiescent U-band luminosity. Any subsequent variations below this value were reset to the quiescent luminosity. The top panel of Figure 13 illustrates this sequence. The bottom panel shows the time integral of the corrected U band luminosity, overlaid on the X-ray luminosity variations. Both the X-ray light curve and integrated U-band luminosity have had estimates of the quiescent luminosity subtracted. The integrated U-band luminosity does show a gradual increase during the corresponding gradual increase of the X-ray flare, yet the peak of the X-ray variations occurs prior to a small plateau in the optical energy. There is a complete breakdown in the apparent relation between the two after this, however; the presence of optical enhancements after the peak of the X-ray flare accounts for the increase in the integrated optical luminosity. It appears that the Neupert effect does not provide a wholly satisfying framework on which to interpret such variations.

For the impulsive X-ray flare shown in Figure 11 the Neupert effect can be investigated by comparing the time derivative of the X-ray variations with the instantaneous optical/radio light curve. We compared the time derivative of the X-ray light curve with the optical variations; there is no correspondence and thus it appears that the U band data do not track the start of the X-ray flare.

As spectacular as the optical/radio flare depicted in the right panel of Figure 11 is, it is even more remarkable that no X-ray flare seems to occur within the tens of minutes

on either side of the time of peak flux enhancement. There is inconclusive evidence of extended chromospheric emission during the flare, and a definite lack of thermal coronal flare emission. One possible explanation for the lack of an X-ray signature follows from the long observed timescales for radiative decay of the radio emission, which implies low ambient electron densities (for particle energies of a few hundred keV, n_e would be $\sim 10^8 \text{ cm}^{-3}$). The n_e^2 dependence of the thermal X-ray emission preferentially biases high density structures; quiescent X-ray structures in active M dwarfs have $n_e \geq 10^{10} \text{ cm}^{-3}$ at temperatures $T_e \geq 3\text{MK}$ (van den Besselaar et al. 2003) and would explain why X-ray flare emission from lower density structures wasn't seen. Another possibility invokes heating at lower temperatures than probed by Chandra: a stellar analogue of solar transition region explosive events (Dere et al. 1989). Ayres et al. (2001) interpreted an enhancement in transition region emission and observed lack of X-ray (and radio) signature on the active binary system HR 1099 as a possible stellar analogue of such an event. Another alternative could be excellent trapping efficiency of the radio loop, so that very few particles precipitate from the trap to heat the surrounding chromosphere and produce subsequent evaporation. An exotic energy budget could also be invoked, where most of the energy goes into accelerating particles (perhaps protons) which would allow deeper penetration of the photosphere and produce continuum emission, but no line emission nor significant evaporation. While we have no conclusive answer to the puzzling flare examined here, it is an example of a unique kind of stellar flare which needs to be considered in the zoo of stellar flare phenomena.

The temporal association between the two UV flares and two corresponding X-ray flares depicted in Figure 12 invites the interpretation that they are causally related. Flare-related enhancement in UV line emission can arise from a deposition of nonthermal energy, as both observations of solar flares (Cheng 1999) and theory of stellar flares (Hawley & Fisher 1992) suggest. If this is the case, then the UV flares are a proxy for nonthermal energy deposition. We could not successfully use the Neupert effect interpretation to explain the temporal relationship between the UV/X-ray flares seen here, however, as there is a large mismatch between the timescales over which the UV flares operate (4-5 minutes) and the timescales for the decay of the X-ray radiation (2–3 hours). The UV/X-ray emissions could still be manifestations of the same reconnection event, but not with a simple temporal association as the Neupert effect prescribes.

4.3. Flare Statistics: Causal Connections based on Temporal Associations

The astounding lack of correlation between flares seen in different wavelength regions in this multi-wavelength flare campaign is puzzling, and we investigated the idea that the

temporal associations are based solely on chance. If the distribution of flares is random in time, then the time between flares (waiting time distribution) should also be a random process, and described by a probability density distribution of the form $P(\Delta t) = \lambda e^{-\lambda \Delta t}$, where Δt is the time between flares and λ is the mean flaring rate. The waiting time distribution has been studied for the case of solar flares and stellar optical flares, and is consistent with a Poisson distribution for small waiting times (Wheatland 2000; Lacy et al. 1976). The probability of observing N flares given a time interval Δt , with mean flaring rate λ is then $P(N; \Delta t, \lambda) = e^{-\lambda \Delta t} (\lambda \Delta t)^N / N!$. If flaring in two disparate wavelength regions occurs independently, then we can multiply the individual probabilities together to estimate the likelihood of seeing such a temporal association by chance.

The X-ray flaring rate determined from the Chandra data described here (0.32 flares hr^{-1}) is consistent with U band flaring rate range of 0.10–0.40 flares hr^{-1} found by Leto et al. (1997) for EV Lac. There is an apparent disconnect with the optical flaring rate estimated during our campaign: ~ 11 optical flares in 8.6 hours, or 1.3 flares hr^{-1} (clouds prevent an accurate count). The flaring rate in the UV is less certain due to the small time coverage (2 flares in ~ 3 hrs), but we estimate it as 0.66 flares hr^{-1} . The radio flaring rate is likewise uncertain, but appears to be greater than 0.09 flares hr^{-1} , due to the one large flare and possibly many small flares observed in ≈ 11 hours. In the 1.5 hour period between 06:30 and 08:00 UT shown in the right panel of Figure 10, there are approximately 9 optical flares and 1 X-ray flare; the probability of a random occurrence of the nine optical flares and one X-ray flare is 4.7×10^{-5} , and yet the Neupert effect in its simplest formulation cannot be used to explain the pattern of energy release. For the ~ 0.5 hr interval between each UV/X-ray flare pair, the probability of having a random flare association between a UV flare and an X-ray flare using the above estimates for the flaring rates is 0.032. As shown in Figure 12, in the six hours from 16:00–24:00 there are 3 X-ray flares and 2 UV flares; the probability of all these flares being randomly associated is 0.026. Thus we cannot reject the hypothesis that the $<$ half-hour interval between the two UV/X-ray flares is due purely to chance, based on the high flaring rate and the low number of UV/X-ray flare associations. Both the optical flare and the radio flare depicted in Figure 11 were large events, and the statistics of the frequency distribution of flare energies in the optical (Leto et al. 1997) suggest a frequency of 0.022 flares hr^{-1} , given an estimated U-band energy of $E_U = 5.2 \times 10^{31}$ erg. The probability of observing an optical flare of this energy and a radio flare, using the estimated radio flare rate from this observation, within 60 s is 5.5×10^{-7} . Thus it appears that the radio and optical flares are not randomly associated, but the lack of a corresponding X-ray flare signature defies our current understanding of stellar flares.

These estimates assume that all flares occur with the same frequency; studies of optical flares reveal that the flare frequency depends on flare energy (Lacy et al. 1976), and investi-

gations of EUV/SXR variations of other M dwarf flare stars (Güdel et al. 2003) also shows a distribution of flare frequencies with flare energy. Therefore, a more detailed treatment of expected and observed multi-wavelength flare associations must be performed before one can assign any significance to one (or two) pairs of flares occurring within a reasonably small amount of time. It is especially important to develop a causal model relating the energies or peak luminosities of flares in different wavelength regions, in order to constrain random associations.

5. Discussion

The study of flare stars continues to reveal new surprises, and our campaign on EV Lac was no exception. The multi-wavelength observations detailed in this paper show both frequent and extreme levels of variability in the dMe flare star EV Lac. At radio wavelengths, we observe highly polarized emission at 6 cm, which we conclude is the signature of coherent emission processes occurring in EV Lac, and supports previous longer wavelength observations showing a large circular polarization signature. We also observed an intense radio outburst which was evident at two frequencies; the timescales and polarization signatures suggest that this is an extreme example of a flare emitting gyrosynchrotron radiation from accelerated particles. The temporal behavior of the spectral index shows large, steep values during the flare rise and peak, suggestive of optically thick conditions. The spectral index is constant for about 40 seconds during the time of radio flare rise; such a signature may be indicative of injection of accelerated electrons into a magnetic trap. The decay of the radio radiation on long timescales is consistent with the trapping of accelerated particles and subsequent energy losses due to Coulomb collisions.

Lee & Gary (2000) demonstrated based on solar flares that a constant spectral index can be obtained from the beginning of particle injection into the flare loop until the time when the maximum number of particles is injected. Lee & Gary (2000) also showed that an initially beamed pitch-angle distribution can result in an offset of the time of maximum of gyrosynchrotron radiation relative to the time of maximum injection; this is due to the extra time needed to fill all the pitch angles required for the resonance condition. This may explain the optical/radio correlations found in our campaign, if the optical emission is a signature of the particle injection, the flattening of the radio spectral index during the 3.6 cm flare rise is related to the injection profile, and the temporal offset of the optical flare maximum from the gyrosynchrotron maximum is a result of beaming in the pitch-angle distribution.

Intense centimetric variations in other M dwarf flare stars are usually accompanied by large values of circular polarization, are shorter lived, and are attributed to coherent

mechanisms; for example, DO Cep (dM4e) was observed by White et al. (1989a) in a radio flare at 6 cm which attained a maximum flux density of 80 mJy ($L_R \sim 1.5 \times 10^{15} \text{ erg s}^{-1} \text{ Hz}^{-1}$), lasting for > 450 seconds. This flare, however, was almost 100% circularly polarized, and was narrow banded, occurring most strongly at 4535 MHz but hardly at 4985 MHz; the star was undetected during a second epoch observation. No emission mechanism was suggested. Stepanov et al. (2001) reported a large amount of circular polarization and flux density (peaking at ≈ 300 mJy, or $L_R \sim 8.7 \times 10^{15} \text{ erg s}^{-1} \text{ Hz}^{-1}$) on AD Leo (dM2e) at 6 cm, which they interpreted as plasma emission; this burst, however, had a very short duration (~ 1 minute). And Benz et al. (1998) saw large amounts of right circular polarization on UV Cet (dM5.5e) at 3.6 cm (maximum Stokes V flux of ~ 30 mJy [$L_R \sim 2.4 \times 10^{14} \text{ erg s}^{-1} \text{ Hz}^{-1}$], total duration ≤ 15 minutes) which Bingham et al. (2001) attributed to emission from a cyclotron maser instability.

There is a signature of highly polarized emission from EV Lac, occurring at 6 cm, with timescales of hours, and peak radio luminosity $L_R \sim 3 \times 10^{13} \text{ erg s}^{-1} \text{ Hz}^{-1}$. This behavior is more similar to the types of enhancements seen in other dMe flare stars which are attributed to a coherent mechanism, yet the variations described here are of smaller luminosity and occur over longer timescales of hours. White et al. (1989a) reported large amounts of circular polarization ($> 80\%$) at 20 cm wavelengths; however EV Lac was undetected in their 6 cm measurements, and there are no other reports of measured circular polarization from this star. The enhancements with large circular polarization signature could be connected to the intense but brief events reported on other active dMe stars.

Several small flares are seen in the optical and ultraviolet. Two small UV enhancements were found during the HST observations. Both had approximately the same enhancement above the surrounding count rate in integrated UV light (and roughly similar durations), and we were able to determine the characteristics of the two flares from line profile variations of bright transition region emission lines. There was no evidence for bulk plasma motions greater than a few km s^{-1} , and the amount of turbulent broadening was different in the two flares.

The X-ray data show a panoply of flare types, with flare timescales ranging from a few minutes to several hours. Analysis of undispersed spectra corresponding to individual flares show no evidence of abundance increases, and only moderate temperature enhancements. For three flares which lasted sufficiently long, we separated the rise phase from the decay phase and found a flare with no temperature increase during the rise, one with a modest temperature increase (7 MK), and a third with a dramatic temperature increase (≥ 30 MK). A comparison of temperature-sensitive emission line ratios in the X-ray grating spectra reveal evidence for higher temperature plasma during flare intervals, with the largest temperatures

occurring during the time intervals with the largest enhancement events. We are able to isolate the shape and level of the continuum emission, and find that it agrees qualitatively with the information derived from the temperature-sensitive line ratios. Abundance-sensitive line ratios cannot constrain the coronal abundance directly, but do suggest a pattern reminiscent of an inverse-FIP effect, as is (now) commonly seen in the coronae of active stars. There is no evidence for large changes in the abundance ratios during times of flares.

In the multi-wavelength flare associations, we find a complete breakdown of expected relations between the signature from accelerated electrons (radio, but secondarily optical and ultraviolet) and the signature presumably due to plasma heating from the accelerated electrons (soft X-ray emission). We find an optical flare coincident with a radio flare to within 54 seconds, which cements the association of optical stellar flares with a bombardment of the lower atmosphere by nonthermal electrons. Particularly puzzling is the lack of an observable X-ray enhancement with this radio/ optical flare, which would have signaled the influence of the nonthermal particles in heating chromospheric material to coronal temperatures via a Neupert effect relationship. Lacking this signature, we can only speculate about the dynamics/characteristics/energy budget of this unusual flare: perhaps the structure involved in the radio/optical flare was of too low an ambient electron density to be an efficient radiator of soft X-rays, and thus was invisible to us.

There are other temporal intervals where optical and UV enhancements could not be connected to contemporaneous X-ray flaring through either timescales or energetics. In only one case can we conclude that a chance superposition of UV and X-ray flares was occurring; in the other, we have no way to explain the correlation using simplistic models. We suggest that a more sophisticated, statistical treatment of multi-wavelength flare correlations is necessary to make causal connections based on temporal associations, particularly for stars (like EV Lac) with high flaring rates.

6. Future Work

The multi-wavelength flare associations described in this paper point to a complex view of the stellar flare process. Flares are found in every wavelength region in which we observed, and yet multi-wavelength correspondences between flares are elusive for all except the largest optical and radio flares. The state of understanding of stellar flares has been riddled with inconsistencies between the solar “paradigm” and stellar reality, which often reveals a confounding set of multi-wavelength interrelationships. Yet the Sun itself is extremely complex, and general trends have only been gleaned after decades of intense study. The stellar community must therefore assess the importance of any one result in light of the

spotty nature of our observing campaigns.

The radio flare presented in this paper has been intriguing, though frustrating, to study, partly due to the choice of radio frequencies and resulting optical depth effects present in the data. This points to the need for radio observations at higher frequencies to establish injection and trapping properties of stellar coronal loops, at frequencies where the emission is predominantly optically thin. With the advent of the Expanded Very Large Array (EVLA), which will have a factor of ~ 10 increase in sensitivity over the current VLA, it will become feasible to perform high time-resolution multi-frequency observations such as those described here, at higher, optically thin, frequencies (15 – 40 GHz) and therefore to probe the dynamics of flares with fewer interpretational ambiguities. In addition, the use of the Atacama Large Millimeter Array (ALMA) at its lowest frequency bandpass (90 GHz) will also stretch coverage of stellar flares, and probe the most energetic flares, with ≈ 100 -fold increase in sensitivity over currently existing mm arrays. The combination of these powerful new radio telescopes, in conjunction with optical and X-ray observations, should provide additional insight into the detailed heating processes operating in stellar flares.

This project presents the results of VLA project AO160. RAO gratefully acknowledges support from SAO grant GO1-2014C and STScI grant HST-GO-8880. SLH and JCA acknowledge funding from HST-GO-8613 from the Space Telescope Science Institute, operated by the Association of Universities for Research in Astronomy, Inc. for NASA. RAO thanks Tim Bastian for fruitful discussions and a careful reading of the paper.

HST(STIS) Chandra(HETGS) VLA McDonald(2.1m) McDonald(2.7m)

REFERENCES

- Abdul-Aziz, H., Abranin, E. P., Alekseev, I. Y., Avgoloupis, S., Bazelyan, L. L., Beskin, G. M., Brazhenko, A. I., Chalenko, N. N., Cutispoto, G., Fuensalida, J. J., Gershberg, R. E., Kidger, M. R., Leto, G., Malkov, Y. F., Mavridis, L. N., Pagano, I., Panferova, I. P., Rodono, M., Seiradakis, J. H., Sergeev, S. G., Spencer, R. E., Shakhovskaya, N. I., & Shakhovskoy, D. N. 1995, *A&AS*, 114, 509
- Ambruster, C. W., Brown, A., Pettersen, B., & Gershberg, R. E. 1994, *Bulletin of the American Astronomical Society*, 26, 866
- Ambruster, C. W., Pettersen, B. R., Hawley, S., Coleman, L. A., & Sandmann, W. H. 1986, in *New Insights in Astrophysics. Eight Years of UV Astronomy with IUE*, 137
- Anders, E. & Grevesse, N. 1989, *Geochim. Cosmochim. Acta*, 53, 197
- Andrews, A. D. & Chugainov, P. F. 1969, *Informational Bulletin on Variable Stars*, 370, 1
- Ayres, T. R., Brown, A., Osten, R. A., Huenemoerder, D. P., Drake, J. J., Brickhouse, N. S., & Linsky, J. L. 2001, *ApJ*, 549, 554
- Baranovskii, E. A., Gershberg, R. E., & Shakhovskoi, D. N. 2001b, *Astronomy Reports*, 45, 309
- Baranovskii, E. A., Gershberg, R. E., & Shakhovskoi, D. N. 2001a, *Astronomy Reports*, 45, 67
- Benz, A. O. *Plasma Astrophysics. Kinetic Processes in Solar and Stellar Coronae*, second edition Institute of Astronomy, ETH Zürich, Switzerland. *Astrophysics and Space Science Library*, Vol. 279, Kluwer Academic Publishers, Dordrecht, 2002.
- Benz, A. O., Conway, J., & Gudel, M. 1998, *A&A*, 331, 596
- Bingham, R., Cairns, R. A., & Kellett, B. J. 2001, *A&A*, 370, 1000
- Bookbinder, J. A., Walter, F. M., & Brown, A. 1992, in *ASP Conf. Ser. 26: Cool Stars, Stellar Systems, and the Sun*, 27
- Caillault, J., Drake, S., & Florkowski, D. 1988, *AJ*, 95, 887
- Cheng, C.-C. 1999, in *The many faces of the sun: a summary of the results from NASA's Solar Maximum Mission.*, 393

- Condon, J. J., Cotton, W. D., Greisen, E. W., Yin, Q. F., Perley, R. A., Taylor, G. B., & Broderick, J. J. 1998, *AJ*, 115, 1693
- Davis, J. E. 2001, *ApJ*, 562, 575
- Delfosse, X., Forveille, T., Perrier, C., & Mayor, M. 1998, *A&A*, 331, 581
- Dennis, B. R. & Zarro, D. M. 1993, *Sol. Phys.*, 146, 177
- Dere, K. P., Bartoe, J.-D. F., & Brueckner, G. E. 1989, *Sol. Phys.*, 123, 41
- Dulk, G. A. 1985, *ARA&A*, 23, 169
- Favata, F., Reale, F., Micela, G., Sciortino, S., Maggio, A., & Matsumoto, H. 2000, *A&A*, 353, 987
- Feldman, U. & Laming, J. M. 2000, *Phys. Scr*, 61, 222
- Feldman, U., Laming, J. M., & Doschek, G. A. 1995, *ApJ*, 451, L79
- Güdel, M., Audard, M., Kashyap, V. L., Drake, J. J., & Guinan, E. F. 2003, *ApJ*, 582, 423
- Güdel, M., Audard, M., Skinner, S. L., & Horvath, M. I. 2002, *ApJ*, 580, L73
- Gagne, M., Valenti, J., Johns-Krull, C., Linsky, J., Brown, A., & Gudel, M. 1998, in *ASP Conf. Ser. 154: Cool Stars, Stellar Systems, and the Sun*, 1484
- Gershberg, R. E. & Chugainov, P. F. 1969, *Izv. Krym. Astrofiz. Obs.*, 40, 7
- Grevesse, N. & Sauval, A. J. 1998, *Space Science Reviews*, 85, 161
- . 1999, *A&A*, 347, 348
- Güdel, M., Benz, A. O., Schmitt, J. H. M. M., & Skinner, S. L. 1996, *ApJ*, 471, 1002
- Hünsch, M., Schmitt, J. H. M. M., Sterzik, M. F., & Voges, W. 1999, *A&AS*, 135, 319
- Hawley, S. L., Allred, J. C., Johns-Krull, C. M., Fisher, G. H., Abbett, W. P., Alekseev, I., Avgoloupis, S. I., Deustua, S. E., Gunn, A., Seiradakis, J. H., Sirk, M. M., & Valenti, J. A. 2003, *ApJ*, 597, 535
- Hawley, S. L. & Fisher, G. H. 1992, *ApJS*, 78, 565
- Hawley, S. L., Fisher, G. H., Simon, T., Cully, S. L., Deustua, S. E., Jablonski, M., Johns-Krull, C. M., Pettersen, B. R., Smith, V., Spiesman, W. J., & Valenti, J. 1995, *ApJ*, 453, 464

- Hinkle, K., Wallace, L., Valenti, J., & Harmer, D. 2000, Visible and Near Infrared Atlas of the Arcturus Spectrum 3727-9300 Å San Francisco: ASP 2000
- Huenemoerder, D. P., Canizares, C. R., & Schulz, N. S. 2001, *ApJ*, 559, 1135
- Johns-Krull, C. M. & Valenti, J. A. 1996, in ASP Conf. Ser. 109: Cool Stars, Stellar Systems, and the Sun, 609
- Klimchuk, J. A. 2000, *Sol. Phys.*, 193, 53
- Kodaira, K., Ichimura, K., & Nishimura, S. 1976, *PASJ*, 28, 665
- Kundu, M. R., White, S. M., Jackson, P. D., & Pallavicini, R. 1988, *A&A*, 195, 159
- Lacy, C. H., Moffett, T. J., & Evans, D. S. 1976, *ApJS*, 30, 85
- Landolt, A. U. 1973, *AJ*, 78, 959
- . 1992, *AJ*, 104, 340
- Lee, J. & Gary, D. E. 2000, *ApJ*, 543, 457
- Leggett, S. K. 1992, *ApJS*, 82, 351
- Lenz, D. D. & Ayres, T. R. 1992, *PASP*, 104, 1104
- Leto, G., Pagano, I., Buemi, C. S., & Rodono, M. 1997, *A&A*, 327, 1114
- Linsky, J. L. & Wood, B. E. 1994, *ApJ*, 430, 342
- Melrose, D. B. & Brown, J. C. 1976, *MNRAS*, 176, 15
- Neidig, D. F. 1989, *Sol. Phys.*, 121, 261
- Neidig, D. F. & Kane, S. R. 1993, *Sol. Phys.*, 143, 201
- Osten, R. A., Ayres, T. R., Brown, A., Linsky, J. L., & Krishnamurthi, A. 2003, *ApJ*, 582, 1073
- Pomerance, B. H., Abbott, B., & Ambruster, C. 1995, *Bulletin of the American Astronomical Society*, 27, 838
- Robinson, R. D., Linsky, J. L., Woodgate, B. E., & Timothy, J. G. 2001, *ApJ*, 554, 368

- Saar, S. H. 1994, in IAU Colloquium 143 Poster Session: The Sun as a Variable Star: Solar and Stellar Irradiance Variations, eds. J.M. Pap, C. Frolich, H.S. Hudson, and S. Solanki, (Cambridge: Cambridge Univ. Press), 147
- Schmitt, J. H. M. M. 1994, *ApJS*, 90, 735
- Sciortino, S., Maggio, A., Favata, F., & Orlando, S. 1999, *A&A*, 342, 502
- Slee, O. B., Willes, A. J., & Robinson, R. D. 2003, *Publications of the Astronomical Society of Australia*, 20, 257
- Smith, R. K., Brickhouse, N. S., Liedahl, D. A., & Raymond, J. C. 2001, *ApJ*, 556, L91
- Stepanov, A. V., Kliem, B., Zaitsev, V. V., Fürst, E., Jessner, A., Krüger, A., Hildebrandt, J., & Schmitt, J. H. M. M. 2001, *A&A*, 374, 1072
- Tull, R. G., MacQueen, P. J., Sneden, C., & Lambert, D. L. 1995, *PASP*, 107, 251
- van den Besselaar, E. J. M., Raassen, A. J. J., Mewe, R., van der Meer, R. L. J., Güdel, M., & Audard, M. 2003, *A&A*, 411, 587
- Watko, J. A. & Klimchuk, J. A. 2000, *Sol. Phys.*, 193, 77
- Wheatland, M. S. 2000, *ApJ*, 536, L109
- White, S. M., Jackson, P. D., & Kundu, M. R. 1989, *ApJS*, 71, 895
- White, S. M., Kundu, M. R., & Jackson, P. D. 1989, *A&A*, 225, 112
- Wood, B. E., Harper, G. M., Linsky, J. L., & Dempsey, R. C. 1996, *ApJ*, 458, 761

Table 1. DECAY TIMESCALES FOR RADIO FLARE

| Time Interval ^a (hr) | X-band = 3.6 cm = 8.4 GHz (s) | C-band = 6 cm = 4.9 GHz (s) |
|------------------------------------|----------------------------------|--------------------------------|
| 8.51–8.54 | 860±70 | ... ^b |
| 8.54–8.90 | 1524±14 | 2728±78 |
| 8.96–9.44 | 2250±45 | 3055±114 |
| 9.51–9.98 | 2546±115 | 3673±283 |
| 10.04–10.52 | 4604±472 | 5510±798 |
| 10.59–11.06 | 3250±229 | 10427±1880 |
| 11.13–11.58 | 4356±465 | 16040±4687 |

^aUT hours on 20 September 2001

^b6 cm emission peaks \approx 130 seconds following 3.6 cm peak

Table 2. STRONG UV EMISSION LINES

| Ion | $\log_{10} T_{\text{form}}$ (K) | λ_{lab} (Å) | desig. ^a | v (km/s) | FWHM (km/s) | ζ_{turb} (km/s) | $f \times 10^{14}$ (erg cm ⁻² s ⁻¹) |
|--------|------------------------------------|-------------------------------|---------------------|-------------|----------------|---------------------------------|---|
| Si III | 4.5 | 1206.510 | Qn | -1±1 | 45±2 | 26.5 | 2.28±0.07 |
| | | | F ₁ | 14±6 | 34±15 | 19.6 | 1.82±0.67 |
| | | | F ₂ | -7±5 | 66±12 | 39.0 | 5.46±0.82 |
| N V | 5.3 | 1238.821 | Qn | -4.4±0.6 | 31±2 | ... | 1.49±0.04 |
| | | | Qb | -1±2 | 70±7 | 36.2 | 1.08±0.05 |
| | | | F ₁ | 5±4 | 34±9 | ... | 1.66±0.37 |
| | | | F ₂ | -1±3 | 29±6 | ... | 1.59±0.31 |
| Si IV | 4.8 | 1393.755 | Qn | -0.2±0.6 | 29±2 | 12.6 | 1.23±0.04 |
| | | | Qb | 9±3 | 109±9 | 64.2 | 1.08±0.08 |
| | | | F ₁ | 2±1 | 25±3 | 8.9 | 4.92±0.45 |
| | | | F ₂ | -2±2 | 44±4 | 23.1 | 5.53±0.46 |
| Si IV | 4.8 | 1402.773 | Qn | -2.1±0.5 | 29±2 | 15.3 | 0.82±0.03 |
| | | | Qb | 12±8 | 126±23 | 75 | 0.44±0.06 |
| | | | F ₁ | 3±1 | 22±3 | 9.7 | 2.55±0.32 |
| | | | F ₂ | -6±2 | 47±5 | 26.8 | 3.96±0.39 |
| C IV | 5.0 | 1548.202 | Qn | -0.4±0.4 | 34±1 | 11.7 | 0.54±0.10 |
| | | | Qb | 1±2 | 135±10 | 79.5 | 2.72±0.20 |
| | | | F ₁ | 0±2 | 35±4 | 12.6 | 10.67±1.07 |
| | | | F ₂ | -3±3 | 53±6 | 27.3 | 11.05±0.98 |
| C IV | 5.0 | 1550.774 | Qn | -3.4±0.7 | 31±2 | 8.0 | 2.64±0.09 |
| | | | Qb | 10±6 | 91±16 | 51.9 | 1.18±0.15 |
| | | | F ₁ | -5±3 | 37±7 | 14.5 | 6.08±0.97 |
| | | | F ₂ | 0±4 | 58±8 | 30.8 | 8.69±1.06 |

^aQn=narrow component of quiescence, Qb=broad component of quiescence
F₁=flare in 1st HST orbit; F₂=flare in 3rd HST orbit (see Figure 1).

Table 3. CHANDRA X-RAY FLARE PROPERTIES ON 20 SEPTEMBER 2001

| Flare # ^a | Time of peak hh:mm (UT) | Peak luminosity ^b (10^{28} erg s ⁻¹) | Δt_{flare} (s) | E_{flare} (10^{31} erg) | τ_d (s) |
|----------------------|----------------------------|---|----------------------------------|--|-----------------|
| 1 | 07:02 | 7.7 | 5900 | 7.8 | 1730±170 |
| 2 | 08:09 | 28.7 | 900 | 0.21 | 112±26 |
| 3 | 09:20 | 2.3 | 7796 | ... | 5180±3400 |
| 4 | 10:19 | 3.9 | 3167 | 5.6 | 780±170 |
| 5 | 12:27 | 3.4 | 4636 | ... | 2850±600 |
| 6 | 14:02 | 5.4 | 5473 | 3.4 | 950±260 |
| 7 | 16:43 | 16.6 | 1611 | ... | 690±90 |
| 8 | 17:17 | 12.7 | 8819 | 43. | 3800±780 |
| 9 | 20:17 | 5.4 | 14130 | 20. | 4140±1210 |

^aFlare numbers are assigned in Figure 7.

^bEstimate of quiescent luminosity, 1.8×10^{28} erg s⁻¹, has been subtracted.

Table 4. X-RAY FLARE SPECTRAL PROPERTIES

| Time ^a | α | kT ₁ (MK) | EM ₁ (10 ⁵¹ cm ⁻³) | kT ₂ (MK) | EM ₂ (10 ⁵¹ cm ⁻³) | Z | χ^2 (dof) |
|-------------------|---|-------------------------------------|---|--------------------------------------|---|--|----------------|
| Q | 0.233 ^{+0.019} _{-0.007} | 4.3 ^{+0.1} _{-0.6} | 5.4 ^{+1.6} _{-0.7} | 9.2 ^{+0.4} _{-0.4} | 5.6 ^{+0.6} _{-2.5} | 0.24 ^{+0.01} _{-0.02} | 124.1 (90) |
| Flare 1 | 0.53 ^{+0.26} _{-0.23} | 3.9 ^{+1.5} _{-0.7} | 2.9 ^{+1.2} _{-1.0} | 13.7 ^{+1.7} _{-1.4} | 4.1 ^{+5.1} _{-1.7} | 0.19 ^{0.3} _{-0.07} | 26.7 (27) |
| Flare 4 | 0.35 ^{+0.29} _{-0.07} | 4.3 ^{+1.0} _{-0.6} | 4.9 ^{+1.6} _{-1.6} | 12.3 ^{+1.7} _{-1.2} | 5.9 ^{+1.3} _{-3.6} | 0.21 (0.12–0.32) | 28.9 (33) |
| Flare 5 | 1 ⁺⁰ _{-0.25} | 3.6 ^{+0.8} _{-0.8} | 2.6 ^{+1.9} _{-1.3} | 10.0 ^{+1.6} _{-1.8} | 1.6 ^{+2.3} _{-0.9} | 0.26 ^{+0.54} _{-0.15} | 21.1 (15) |
| Flare 6 | 0.58 ^{+0.21} _{-0.27} | 4.3 ^{+1.6} _{-0.6} | 4.7 ^{+3.4} _{-2.1} | 12.4 ^{+2.7} _{-1.7} | 3.0 ^{+5.6} _{-1.7} | 0.17 ^{+0.41} _{-0.1} | 19.5 (23) |
| Flare 8 | 0.60 ^{+0.4} _{-0.09} | 3.7 ^{+0.3} _{-0.5} | 1.0 ^{+0.7} _{-0.4} | 30.0 ^{+3.4} _{-5.1} | 2.6 ^{+1.2} _{-1.7} | b | 47.5 (49) |
| Flare 9 | 0.45 ^{+0.13} _{0.03} | 4.5 ^{+0.1} _{-0.4} | 4.2 ^{+1.2} _{-0.9} | 18.6 ^{+2.9} _{-1.6} | 2.2 ^{+0.2} _{-0.9} | c | 87.1 (70) |
| Flare1 Rise | 0.47 ^{+0.5} _{-0.35} | 3.6 ^{+0.7} _{-0.6} | 92.4 ^{+557.6} _{-92.4} | X ^e | X ^e | f | 5.0 (4) |
| Flare1 Decay | 1 ⁺⁰ _{-0.35} | 3.9 ^d | 2.9 ^d | 16.9 ^{+3.7} _{-2.2} | 67.8 ^{+15.4} _{-18.5} | 0.16 ^{+0.25} _{-0.09} | 18.7 (19) |
| Flare8 Rise | 0.51 ^{+0.49} _{-0.44} | 35 ⁺¹⁰⁹ ₋₁₂ | 10.2 ^{+6.7} _{-10.2} | X ^e | X ^e | 1 ^d | 3.4 (3) |
| Flare8 Decay | 0.56 ^{+0.04} _{-0.02} | 3.9 ^{+1.0} _{-0.7} | 9.1 ^{+3.1} _{-3.8} | 13.8 ^{+1.5} _{-1.0} | 11.3 ^{+1.7} _{-3.3} | 0.17 ^{+0.09} _{-0.07} | 70.2 (45) |
| Flare9 Rise | 0.26 ^{+0.45} _{-0.16} | 6.8 ^{+1.1} _{-1.5} | 15.1 ^{+203.6} _{-10.8} | X ^e | X ^e | 0.08 ^{+0.18} _{-0.06} | 1.8 (5) |
| Flare9 Decay | 0.50 ^{+0.11} _{-0.04} | 3.8 ^{+0.6} _{-0.3} | 6.7 ^{+1.9} _{-1.8} | 11.4 ^{+0.8} _{-0.5} | 6.5 ^{+0.8} _{-2.7} | 0.20 ^{+0.04} _{-0.05} | 77.1 (64) |

^aTime intervals shown in Figure 7.

^bVariable abundance APEC model fit w/following abundance constraints: O 0.82^{+0.68}_{-0.58}, Ne 4.63^{+2.29}_{-2.88}, Mg 4.92^{+6.48}_{-3.73}, Fe 0.94^{+0.97}_{-0.68}

^cVariable abundance APEC model fit w/following abundance constraints: O 0.37^{+0.17}_{-0.06}, Ne 1.06^{+0.32}_{-0.13}, Mg 0.77^{+0.36}_{-0.41}, Fe 0.28^{+0.10}_{-0.02}

^dParameter fixed at value given

^eParameter omitted from model fit

^fVariable abundance APEC model fit w/following abundance constraints: Ne $0.49^{+1000}_{-0.36}$, other abundances $0.08^{+9.22}_{-0.075}$

Table 5. STRONG EMISSION LINES IN X-RAY SPECTRA

| Ion | Wavelength (Å) | Q — Flux $\times 10^{14}$ erg cm $^{-2}$ s $^{-1}$ — | Large Flares ^a | Small Flares ^a |
|---------|-------------------|---|---------------------------|---------------------------|
| Si XIV | 6.18 | 2.16 \pm 0.64 | 15.3 \pm 2.14 | 6.05 \pm 0.85 |
| Si XIII | 6.65 | 4.25 \pm 0.74 | 12.2 \pm 1.79 | 9.84 \pm 0.92 |
| Mg XII | 8.42 | 2.25 \pm 0.61 | 7.46 \pm 1.59 | 3.18 \pm 0.66 |
| Mg XI | 9.17 | 2.98 \pm 0.54 | 4.62 \pm 1.28 | 3.62 \pm 0.58 |
| Ne X | 12.13 | 25.70 \pm 1.66 | 53.1 \pm 3.47 | 35.6 \pm 1.85 |
| Ne IX | 13.45 | 22.8 \pm 1.77 | 23.9 \pm 3.10 | 23.9 \pm 1.87 |
| Fe XVII | 15.01 | 20.4 \pm 2.4 | 28.5 \pm 4.10 | 19.7 \pm 2.18 |
| O VIII | 18.97 | 64.2 \pm 4.59 | 73.7 \pm 7.82 | 65.7 \pm 4.29 |
| O VII | 21.60 | 16.30 \pm 3.56 | 17.60 \pm 6.04 | 19.8 \pm 3.43 |

^a“Large Flares” = flares 1,2,7,8; “Small Flares” = flares 3–6,9 demarcated in Figure 7.

Table 6. TEMPERATURE-SENSITIVE EMISSION LINE RATIOS IN X-RAY SPECTRA

| Ratio ^a | Q | Large Flares | Small Flares |
|--------------------------|--|--|---|
| Si XIV 6.18/Si XIII 6.45 | 0.51 \pm 0.18 10.3 MK 9.3<T<11.4 | 1.25 \pm 0.25 14. MK 12.9<T<14.9 | 0.62 \pm 0.10 11.1 MK 10.4<T<11.6 |
| Mg XII 8.42/Mg XI 9.17 | 0.76 \pm 0.25 7.4MK 6.5<T<7.9 | 1.61 \pm 0.56 9.3MK 8.1<T<10.3 | 0.88 \pm 0.23 7.7MK 7.0<T<8.2 |
| Ne X 12.13/Ne IX 13.45 | 1.13 \pm 0.11 4.7MK 4.6<T<4.9 | 2.22 \pm 0.32 5.6MK 5.6<T<6.2 | 1.49 \pm 0.14 5.2MK 4.9<T<5.3 |
| O VIII 18.97/O VII 21.60 | 3.94 \pm 0.90 3.7MK 3.4<T<4.0 | 4.19 \pm 1.50 3.8MK 3.2<T<4.3 | 3.32 \pm 0.61 3.5MK 3.2<T<3.7 |

^aEnergy flux ratios

Table 7. ABUNDANCE-SENSITIVE EMISSION LINE RATIOS IN X-RAY SPECTRA

| Ratio ^a | FIP type ^b | APEC ^c | Q | Large Flares | Small Flares |
|--------------------------|-----------------------|-------------------|-------------|--------------|--------------|
| Si XIII 6.65/Mg XII 8.42 | LL | 1.06 | 1.9±0.6 | 1.6±0.4 | 3.1±0.7 |
| Fe XVII 15.01/Mg XI 9.17 | LL | 10.5 | 6.84±1.47 | 6.17±1.92 | 5.44±1.06 |
| Mg XI 9.17/Ne X 12.13 | LH | 0.32 | 0.116±0.003 | 0.087±0.003 | 0.102±0.002 |
| Fe XVII 15.01/Ne X 12.13 | LH | 4.1 | 0.79±0.11 | 0.54±0.08 | 0.55±0.07 |
| Ne IX 13.45/O VIII 18.9 | HH | 0.19 | 0.36±0.04 | 0.32±0.05 | 0.36±0.04 |

^aEnergy flux ratios

^b=low FIP (<10 eV), H=high FIP (>10 eV)

^ctheoretical value using abundances of Grevesse & Sauval (1998, 1999).

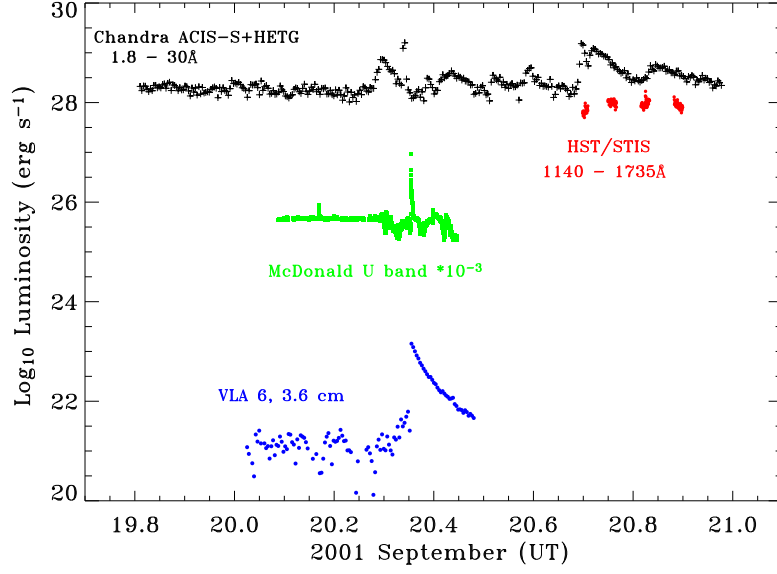


Fig. 1.— Timeline of observations for the 2001 September flare campaign; luminosities in each waveband are plotted to gauge the large-scale variations encountered. The *Chandra* X-ray pointing, lasting 100ks, formed the core of the campaign and was supplemented by ultraviolet, optical, and radio observations.

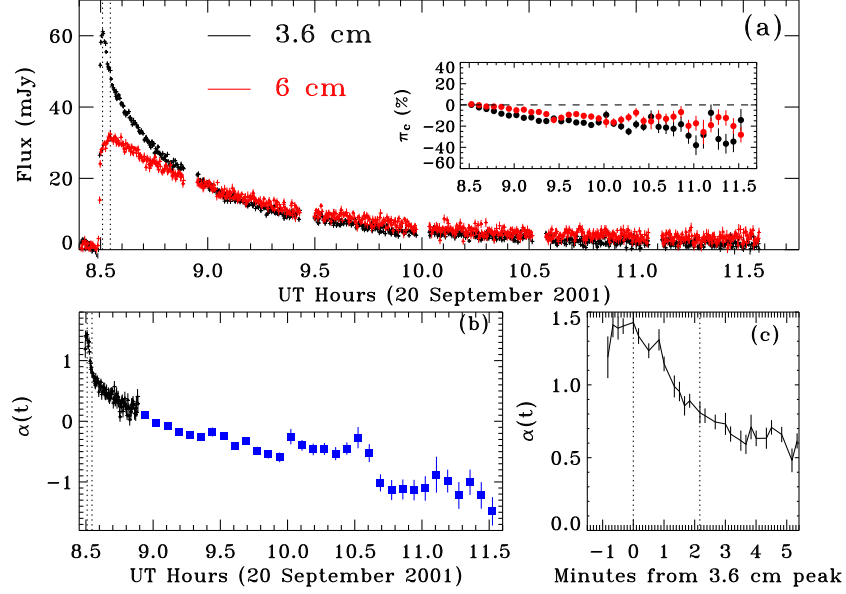


Fig. 2.— **(a)** Variations of total flux density at 3.6 (black) and 6 cm (red) near the time of the large radio flare on 20 September 2001. Each tick corresponds to 10 seconds, the temporal resolution available with the VLA. 1σ error bars are plotted. The inset shows variation of percent circularly polarized radiation in 300 second intervals at both frequencies during the decay of the flare; dashed line indicates zero polarization. **(b)** Variation of spectral index α , $S_\nu \propto \nu^\alpha$, between 6 and 3.6 cm ($S_\nu \propto \nu^\alpha$). Crosses indicate data sampling of 10 seconds; blue squares indicate data sampling of 5 minutes (300 seconds). 1σ uncertainty on spectral slope is also plotted. **(c)** Detailed examination of spectral index variations of the few minutes around the flare rise and peak: the spectrum appears to flatten for about 40 seconds before the 3.6 cm peak. Dotted lines for all panels indicate times of 3.6 and 6 cm peaks (3.6 cm peaks first).

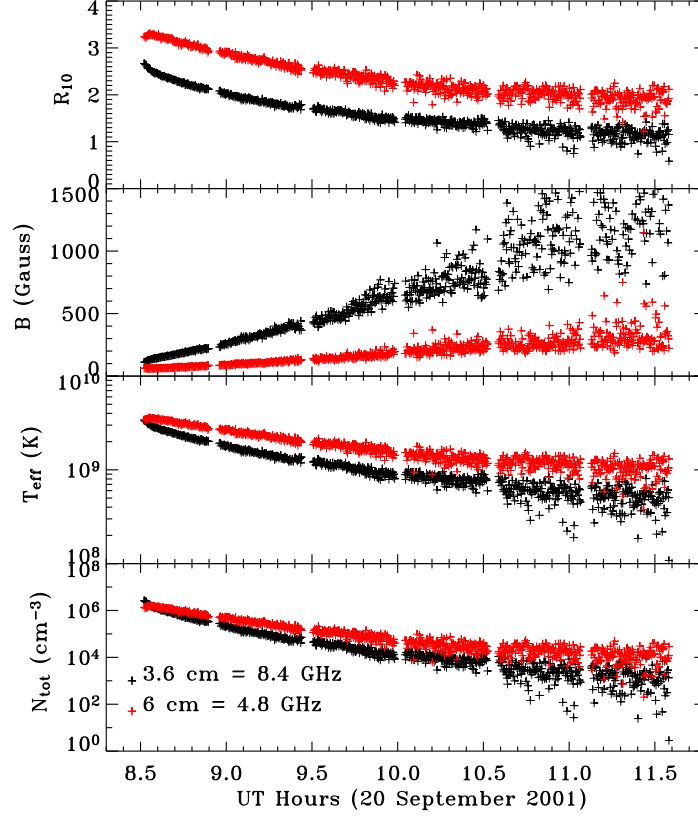


Fig. 3.— Model parameters derived during the decay of a large radio flare, under the assumption of optically thick gyrosynchrotron emission from an inhomogeneous, dipole magnetic field configuration. R_{10} is the source size in 10^{10} cm, B the magnetic field strength of the radio-emitting source, T_{eff} the effective temperature of the plasma, and N_{tot} the total number density of nonthermal electrons above a cutoff value of 10 keV; see text for details.

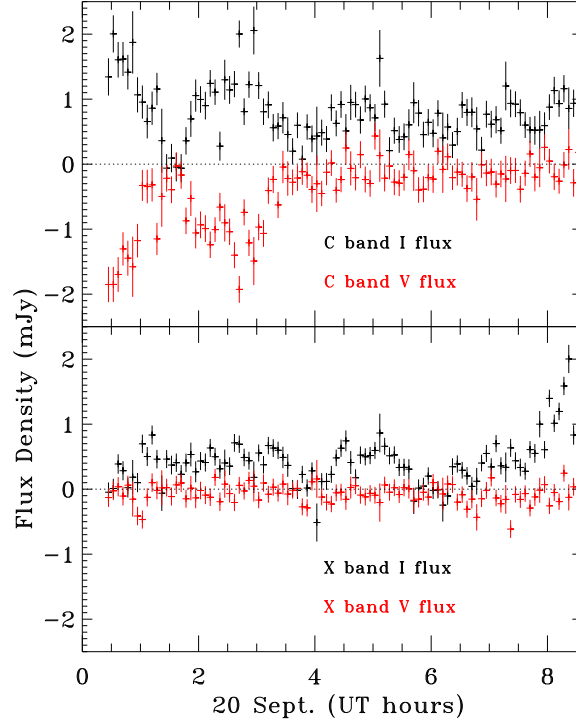


Fig. 4.— **(top)** Variation of total intensity (I) and circularly polarized flux (V) at C band (6 cm) during the first 8 hours of the VLA observation; data has been binned to 300 second intervals. Two events characterized by enhanced I and V fluxes are noticeable. **(bottom)** Variations of total intensity (I) and circularly polarized flux (V) at X band (3.6 cm) during the first 8 hours of the VLA observation. The variability seen at C band is not seen at this higher frequency; binning is same as above.

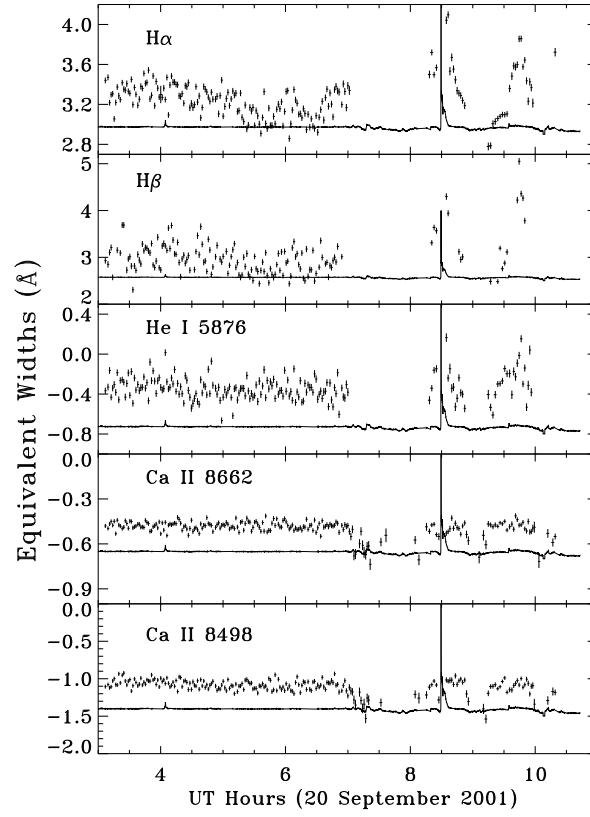


Fig. 5.— Variation of equivalent widths of H α , H β , He I λ 5876, and Ca II $\lambda\lambda$ 8662,8498. Overplotted is the U band light curve.

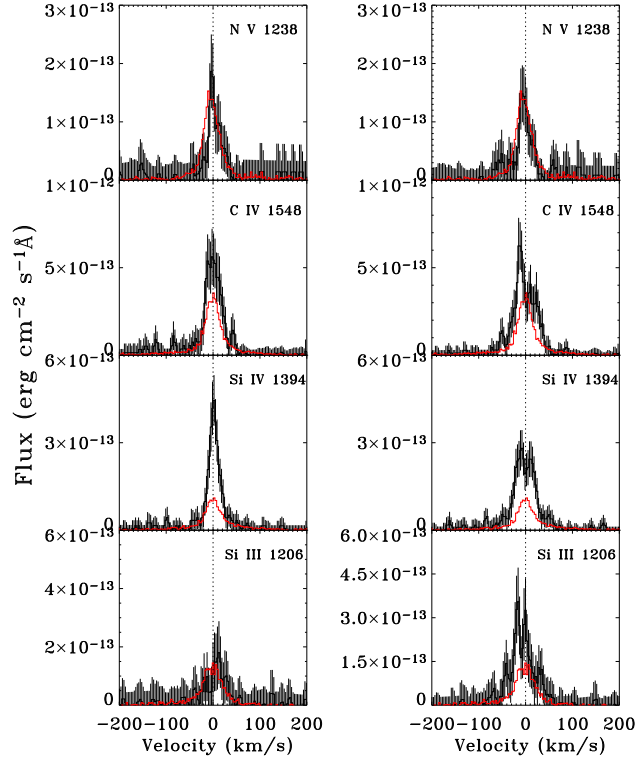


Fig. 6.— **(left)** Variation of strong UV emission lines during a small flare in the first orbit of HST observations. Overplotted in red is the line profile corresponding to quiescent times. This flare lasted 4 minutes, with a peak enhancement of about 1.5 times the neighboring count rates. **(right)** Same as left panel, for a small flare in the third orbit of HST observations. This flare lasted ~ 5 minutes, with a peak enhancement of about 1.8 times the neighboring count rates. The formation temperatures of the lines decrease downward. Flare spectra have been smoothed over two wavelength bins.

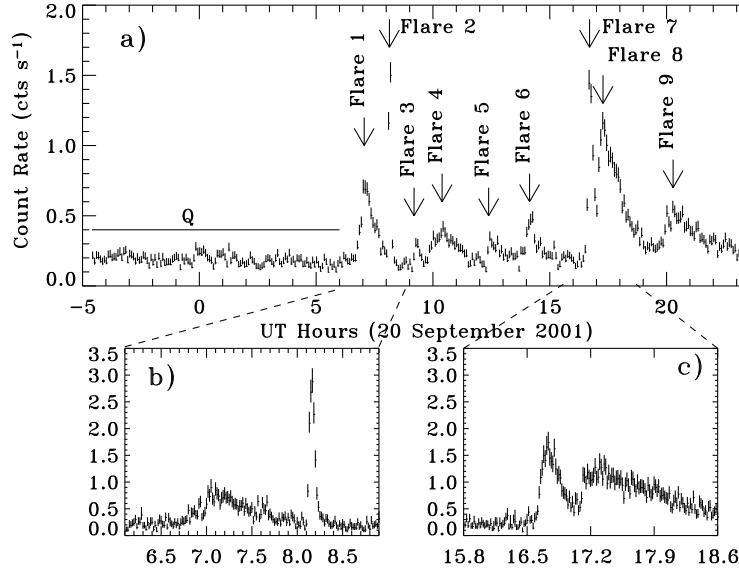


Fig. 7.— (a) Light curve of *Chandra* MEG data. Each tick mark represents an average over 300 seconds of data; error bars span $\pm 1 \sigma$ uncertainties of the count rate. At least nine large (factor of > 2 enhancement over quiescent) flares are noticeable. Panels (b) and (c) detail two impulsive flares; the time binning is 60 seconds. Flare 2 lasts at most 8 minutes, with peak count rate ~ 15 times the quiescent count rate, while flare 7 lasts 25 minutes with maximum enhancement 8.5.

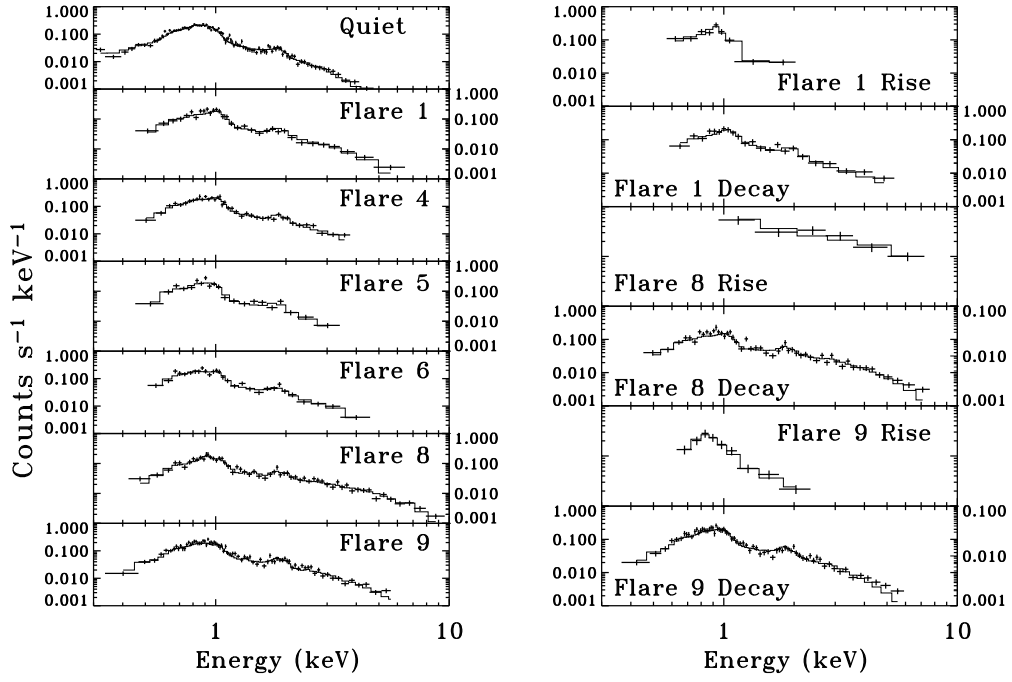


Fig. 8.— ACIS 0th order spectra of differing temporal regions (defined in Figure 7). Crosses indicate data points and errors; histograms illustrate model fit to spectra. Model parameters are indicated in Table 4. Left panels illustrate spectra accumulated in broad activity bins, corresponding to individual flares (or quasi-steady conditions); right panels attempt to differentiate changing spectral conditions during individual flares with sufficient durations.

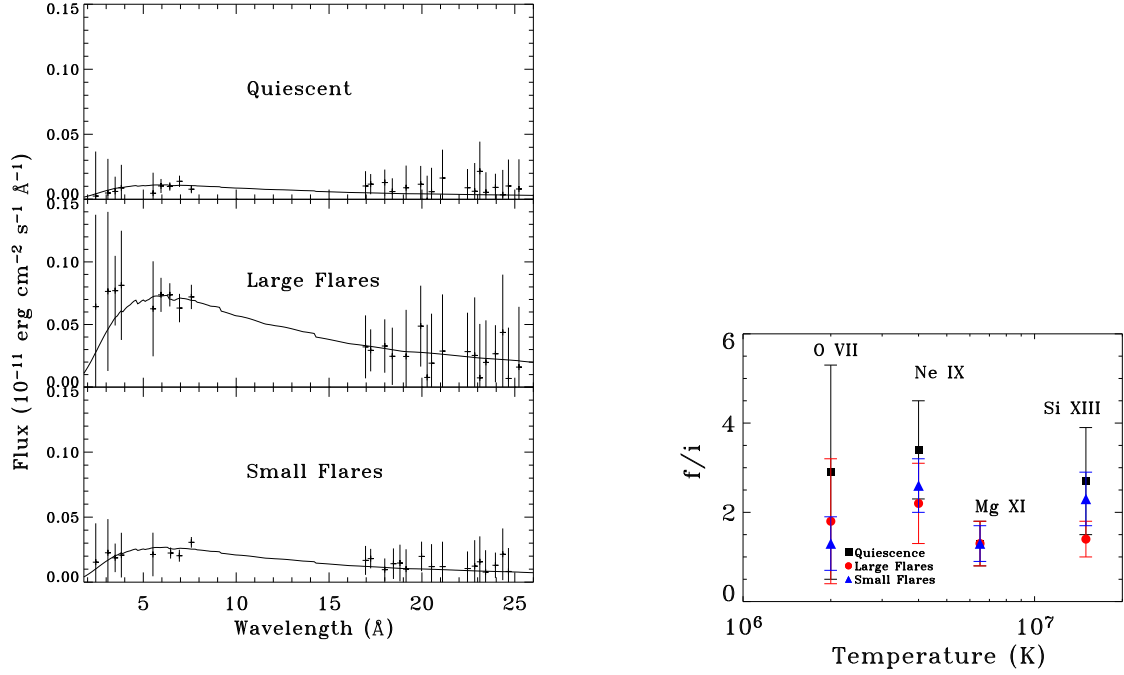


Fig. 9.— **(left)** X-ray continuum spectra during (top) quiescence, (middle) large flares (flares 1,2,7 and 8), and (bottom) smaller flares (flares 3–6 and 9). The intervals encompassing large enhancement flares show an increase in short wavelength continuum flux, associated with creation of high temperature plasma. The intervals encompassing small enhancement flares also shows a slight increase compared with quiescence, signaling the existence of hot plasma during these flares. Also shown with a solid line for all three spectra is a schematic continuum spectrum, formed from plasma at $T \sim 12$ MK, and scaled to the observed continuum fluxes at wavelengths of 10 Å and longer. **(right)** Variation in f/i ratios during three time intervals: quiescence, large flares (flares 1, 2, 7 and 8) and small flares (3–6 and 9). There is no evidence for an increase in electron densities in any of the density-sensitive line ratios, during either flare segment.

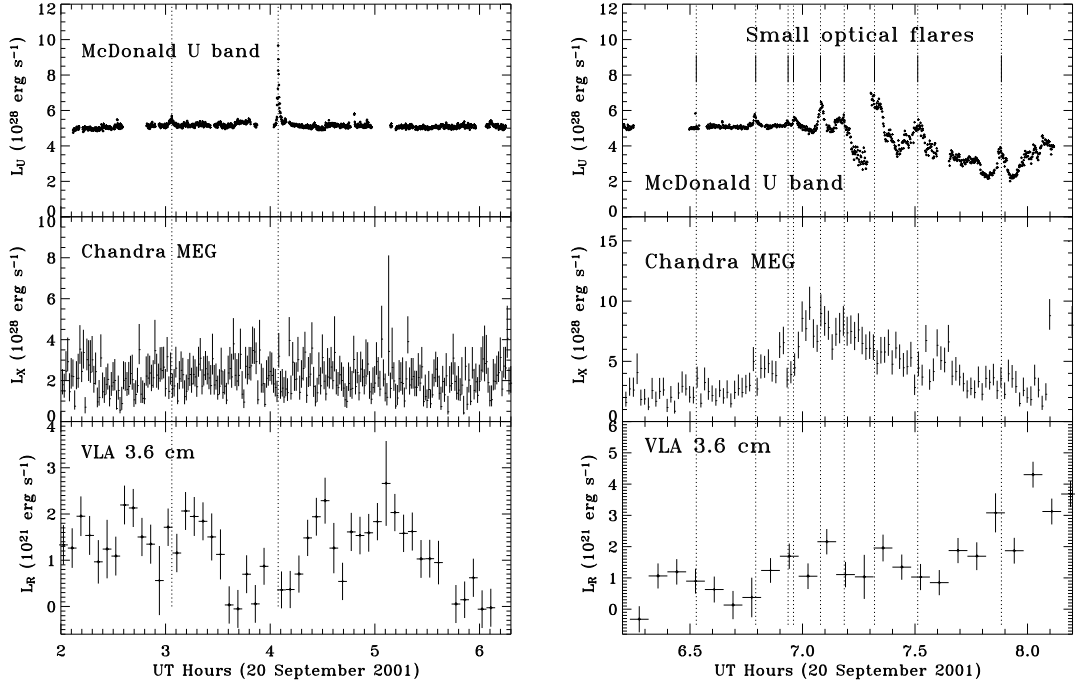


Fig. 10.— Light curves of optical, radio, and X-ray data during time of overlap. Radio binning is 300 seconds; X-ray binning is 60 seconds; optical binning is 2.839 seconds, with a cadence of 7 seconds for multiple filter monitoring and filter wheel rotation. Dotted lines indicate times of peak optical emission.

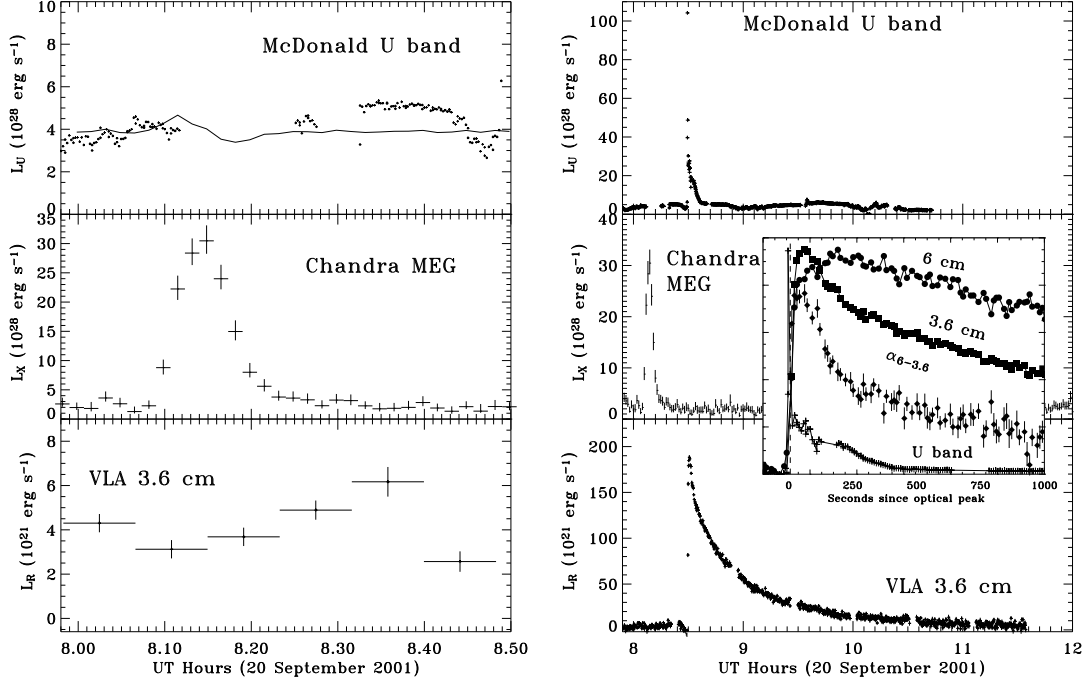


Fig. 11.— Light curves of optical, radio, and X-ray data during time of overlap from 08:00–12:00 UT. X-ray binning is 60 seconds; optical binning is 2.839 seconds with 7 second cadence. In the left panel, radio binning is 300 seconds; in the right panel, it is 10 seconds. The upper left panel overplots the time derivative of the X-ray light curve, to compare against optical variations in light of the Neupert effect. The inset to the right panel details the evolution of an impulsive flare seen at radio and optical wavelengths in normalized flux units. The dashed line indicates the location in the U band light curve where the first derivative changes sign after the flare peak; this may signal a change from the impulsive to gradual phase of the flare. Note that according to this criterion, the radio flares occur during the gradual phase of the flare. The diamonds indicate the spectral index between 6 and 3.6 cm during the initial stages of the decay. See section 4 for more details.

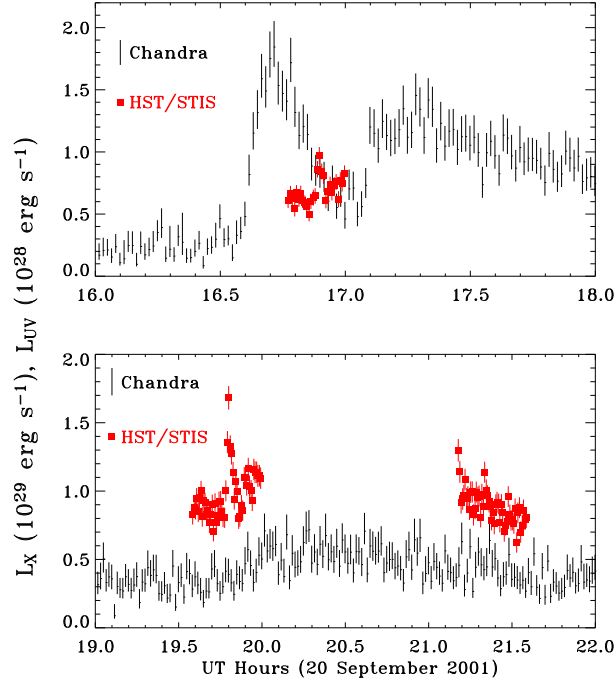


Fig. 12.— Close-up of two small UV enhancements during a time of X-ray flaring activity. Top panel shows X-ray flares 7 and 8; bottom panel, X-ray flare 9. Binning in both light curves is 60 seconds. Lines indicate $\pm 1\sigma$ uncertainties in luminosity. Neither the time scales nor the energetics of the X-ray/UV events is consistent, and appears to be a random association of flares; see text for details.

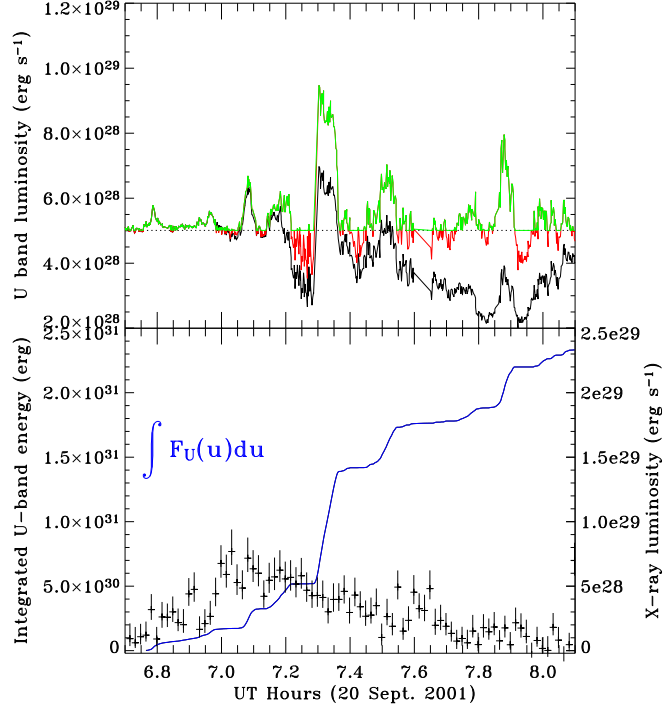


Fig. 13.— **(top)** Optical U band light curve, converted to luminosity (using quiescent luminosity of $5.01 \times 10^{28} \text{ erg s}^{-1}$, shown as dotted line). Black curve shows original data; red curve sketches data after cloud correction. The green curve sets any points falling below the quiescent luminosity equal to it; the red and green curves are equivalent above the quiescent luminosity. **(bottom)** Crosses show the X-ray luminosity variations during the time of a gradual flare (X-ray flare 1 in Figure 7; quiescent luminosity has been subtracted, time binning is 300 seconds) and blue curve delineates the time integral of U band flare luminosity (quiescent luminosity subtracted). The profile of the integrated U band luminosity does not match the instantaneous X-ray luminosity, as one would expect under the Neupert effect (see text).